[9]F. F. Rieke and W. Prepejchal, in *Sixth International Conference on the Physics of Electronic and Atomic Collisions, Cambridge, Massachusetts*, 1969 (MIT U. P., Cambridge, Mass., 1969), p. 623.
[10]H. Bethe, Ann. Physik 5, 325 (1930).
[11]H. Bethe, in *Handbuch der Physik*, edited by H. Geiger and K. Scheel (Springer, Berlin, 1933), Vol. 24/1, p. 273.
[12]M. Inokuti, Rev. Mod. Phys. 43, 297 (1971).
[13]U. Fano, Phys. Rev. 95, 1198 (1954).
[14]R. L. Platzman, J. Phys. Radium 21, 853 (1960).
[15]R. Gold and E. F. Bennett, Phys. Rev. 147, 201 (1966).
[16]K. D. Carlson, P. W. Gilles, and R. J. Thorn, J. Chem. Phys. 38, 2725 (1963).
[17]R. H. Busey and W. F. Giauque, J. Am. Chem. Soc. 75, 806 (1953).
[18]R. L. Platzman, Vortex 23, 372 (1962).
[19]R. L. Platzman, J. Chem. Phys. 38, 2775 (1963).
[20]W. P. Jesse, J. Chem. Phys. 38, 2774 (1963).
[21]M. Inokuti, Y.-K. Kim, and R. L. Platzman, Phys. Rev. 164, 55 (1967).
[22]R. J. Bell and A. Dalgarno, Proc. Phys. Soc. (London) 86, 375 (1965).
[23]R. J. Bell and A. Dalgarno, Proc. Phys. Soc. (London) 89, 55 (1966).
[24]The value is for the ground vibrational and rotational state and is derived from Table VI of L. Wolniewicz, J. Chem. Phys. 45, 515 (1966).
[25]R. L. Platzman, in *Radiation Research* 1966, *Proceedings of the Third International Congress of Radiation Research, Cortina d'Ampezzo, Italy*, 1966, edited by G. Silini (North-Holland, Amsterdam, 1967), p. 20.
[26]B. L. Schram, A. J. H. Boerboom, and J. Kistemaker, Physica 32, 185 (1966); B. L. Schram, *ibid.* 32, 197 (1966); B. L. Schram, M. J. van der Wiel, F. J. de Heer, and H. R. Moustafa, J. Chem. Phys. 44, 49 (1966); J. Schutten, F. J. de Heer, H. R. Moustafa, A. J. H. Boerboom, and J. Kistemaker, *ibid.* 44, 3924 (1966).
[27]M. Inokuti and J. C. Person (unpublished).
[28]I. Santar and J. Bednář, Collection Czech. Chem. Commun. 34, 1 (1969); 34, 311 (1969); I. Santar, in *Progress and Problems in Contemporary Radiation Chemistry*, Vol. 1, edited by J. Teplý (Czechoslovak Academy of Sciences, Prague, 1971), p. 51; in Third Tihany Symposium on Radiation Chemistry, Balatonfüred, Hungary, 1971, Preprint ÚJV 2611-Ch (unpublished).

PHYSICAL REVIEW A VOLUME 6, NUMBER 4 OCTOBER 1972

Extreme-Wing Line Broadening and Cs-Inert-Gas Potentials*

R. E. M. Hedges,† D. L. Drummond, and Alan Gallagher‡
Joint Institute for Laboratory Astrophysics, University of Colorado, Boulder, Colorado 80302
(Received 6 April 1972)

The emission profiles of the cesium resonance lines broadened by collisions with inert gases have been measured from about 50–1000 cm^{-1} from line center. The emission is observed from optically excited Cs in a cell whose temperature is varied from about 300 – 800 °K. By measuring the wing intensity relative to the entire line intensity from optically thin Cs, the profiles can be related to theoretical models without knowledge of the cesium density. The quasistatic theory of line broadening, extended to include the distribution of perturber positions about the Cs^*, is used to analyze the data. The observed temperature dependence of the emission profiles is associated with the temperature dependence of the perturber distribution in the Cs*–inert-gas adiabatic potential. The quasistatic spectrum depends on the difference between excited- and ground-state adiabatic potentials, so each potential is thereby separately determined from the data. The $X\Sigma$, $A\Pi$, and $B\Sigma$ potentials for the 3.5–5-Å region are given.

I. INTRODUCTION

This paper reports measurements and explanations of the far-wing intensities of Cs resonance lines broadened by collisions with inert gases.[1a] We have measured emission from optically excited Cs in a cell whose temperature was varied. The cell contains typically 300 Torr of inert gas. The Cs is optically thin so that the ratio of wing to total emission intensity is meaningful without knowledge of the Cs density. This wing radiation, which we observe for 1000 Å from line center, is essentially a continuum. We describe it here in terms of the molecular radiation of unstable Cs–inert-gas molecules. The population distribution in the free and bound molecular states has a pronounced effect on this extreme-wing intensity distribution and we utilize the temperature dependence as a powerful diagnostic tool. This interpretation of the temperature-dependent wing profiles extends the quasistatic model originally formulated by Holtsmark, and developed by Kuhn, Jablonski, Margenau, Foley, Holstein, and others.[1–3] It allows the experimental data to be understood and unfolded to give the $Cs^*(6\,^2P)$ and $Cs(6\,^2S)$ adiabatic potentials for interaction with the inert gases in

the region from about 3.5 to 5 Å.

In the experiment the Cs excitation temperature is elevated by the optical excitation, but the nuclear motions are in equilibrium with the cell walls. At sufficiently large perturber pressures collisional rates dominate over radiative losses and bound Cs*–inert-gas molecules are formed in a concentration that is also in equilibrium with the kinetic temperature of the cell. The density of perturbers (bound and free) at R from a Cs* is then

$$n(R) = n_0 \exp\{-[V_u(R) - V_u(\infty)]/kT\},$$

where $V_u(R)$ is the Cs*–inert-gas adiabatic potential and n_0 the background inert-gas density.

The quasistatic theory of line broadening identifies wing radiation at frequency ν as arising from an electronic transition that occurred while the nuclei were separated by R, where $V_u(R) - V_l(R) = h\nu$ (u = upper, l = lower). (It neglects the effect of nuclear motion on the spectrum, and is valid only in the line wings.) This relation thus transforms the probability distribution for internuclear separation into the distribution of wing radiation. The exponential temperature dependence of the perturber density at R then appears as temperature dependence at the frequency ν that is produced at that R (see Fig. 1). (In some cases more than one R can produce the same ν, with a resultant mixed temperature dependence. In the case of diatomic interactions this lack of uniqueness does not present serious interpretative problems.) The measured wing temperature dependence thus provides a relation between ν and V_u or between $V_u(R)$ and $V_l(R)$. The temperature dependence will of course be barely discernible if

$$|[V_u(R) - V_u(\infty)]/kT| \ll 1$$

so this diagnostic technique works best in the far wings of lines. Since the wing distribution at one temperature provides, in the quasistatic model, $V_u(R) - V_l(R)$, it is thus possible to separately reconstruct $V_u(R)$ and $V_l(R)$ from the data. (The procedure is described in Sec. IID.) In the quasistatic theory the wing intensity from ν to ν' is due to the perturbers from R to R', but only for the far wing which is due to nearby perturbers. This relation cannot be extended to large R, so the initial radial position is not prescribed. Our adiabatic potentials are therefore not uniquely determined; the radial starting point is needed. Fortunately atomic-beam scattering measurements have provided a $V_l(R)$ for the Cs–inert-gas system, so we have fixed the radial starting point by comparing our $V_l(R)$ to these data. The procedure is outlined in more detail in Sec. IID and in the data-analysis sections.

The inert-gas densities of the experiment are chosen to be low enough to allow the use of binary collision theory, yet high enough to ensure a distribution of bound Cs*–inert-gas molecules in equilibrium with the kinetic temperature. Since free Cs* is optically excited this requires bound molecule formation within the Cs* lifetime of 3×10^{-8} sec. The theory section includes a discussion of the emission spectrum expected from free-particle collisions and from the bound species. The dependence of the wing spectrum on inert-gas density is measured to test for the validity of the assumed equilibrated distribution. The theory section also includes a discussion of the quasistatic theory with emphasis on the particle distribution factors that are normally neglected. The relationships between the absorption and emission spectrums are also reviewed for the purpose of comparison with absorption data from another experiment.

Cesium line broadening due to inert-gas collisions is an old and well documented problem.[1-4] For many years the general wing profile has been

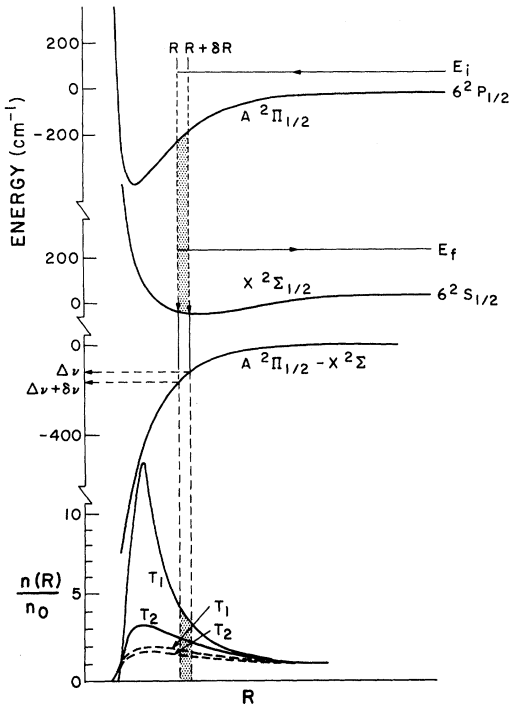

FIG. 1. Diagram of the quasistatic radiation process. The initially excited atom emits $\nu \rightarrow \nu + d\nu$ when a perturber is at $R \rightarrow R + dR$, where $h\nu(R) = V_{\text{upper}}(R) - V_{\text{lower}}(R) = E_i - E_f$. A free-free transition is shown as an example. The proportion of perturbers between R and $R + dR$ in a thermal vapor is $4\pi R^2 dR$ times the $n(R)/n_0$ shown. The solid $n(R)/n_0$ lines are the equilibrium canonical distribution; the dashed lines correspond to only free-particle collisions. The temperature dependence of $n(R)/n_0$ appears in the wing intensity at $\nu(R)$.

a fascinating problem, particularly the red and blue satellites. A number of explanations have been suggested, but the issue has appeared to remain uncertain; i.e., in the quasistatic approximation a difference potential with a minimum will produce a red satellite and one with a maximum a blue satellite, while differently parametrized potentials are used to fit shifts and widths of the line center.[5] It is not apparent what reasonable shaped potentials might lead to the observed red and blue satellites and the observed shifts and widths as well. On the other hand, peculiarities in the bound-free and free-free Franck–Condon factors rather than minima or maxima might cause wing structure (Ref. 6 gives one example). In the absence of restrictive experimental data or theoretical bounds for the potentials, conclusive explanations are hard to produce. Baylis[7] has provided valuable theoretical information about the potentials, but owing to the approximations required for such complex atomic systems experimental verification is needed. The present measurements yield wing profiles in regions heretofore unprobed, and by accurately normalizing to line center and varying the gas temperature we produce very stringent requirements on the potentials. We can explain the observed far wings and blue satellites, but not the familiar red satellites since these are closer to line center than our present data. Or, equivalently, the region of internuclear separation where the red satellites are produced is further out than the region measured here. But we believe that the techniques developed by Baylis for semiempirical calculations of these potentials should be adequate to reliably predict the potentials at larger separations, particularly once we can prescribe their behavior closer in. We hope this will soon lead to a conclusive explanation for the red satellites.

It is well known that knowledge of the interaction potential is necessary for an understanding of many atomic collision processes: Frequently explanations of collisions are uncertain, despite a sophisticated collision theory, because the interaction potential is not known. Phenomena which critically depend on the interaction potential of unstable species include cross sections for excitation transfer, quenching of excited states, spin exchange, and depolarization, Penning ionization, shift and broadening of spectral lines, elastic scattering of atomic beams, chemical reactions, and dissociation processes. Many of these phenomena have been studied for precisely the alkali-metal-atom–inert-gas system being studied here.

Our experiment has close analogies to work on molecular continuum absorption,[8] and to the analysis of the energy distribution of electrons produced by Penning ionization.[9] In the former type of work the repulsive part of the upper-state potential of, e.g., H_2 could be derived from the absorption by H_2 in its ground electronic and vibrational state. In the latter work, the emission of an electron by a vertical jump between potential curves of the He*–target-atom pair is similar to the emission of a photon during the collision of Cs* with an inert-gas atom, except that in Penning ionization the probability of the process taking place is strongly dependent on the internuclear separation.

II. THEORY

A. Spectral Profile

A collisionally broadened line has a Lorentzian (or Voigt) profile near line center, which can be related to the Fourier transform of a radiative wave in which short duration collisions produce sudden phase changes. The theory of this impact-broadened line shape has been extensively developed.[1] The phase shifts, averaged over impact parameters, are dominated by the interaction potentials at much greater internuclear separation than the region which produces the wing radiation studied here. The quasistatic theory of line shapes is applicable far enough into the line wings for the broadening due to nuclear velocity, or finite collision time, to be minor.[1,3] We have measured line shapes in the region of wave-number shifts of 50–1000 cm^{-1} from line center. (Our line-broadening equations are in traditional frequency units, but we will express the data throughout in wave numbers.) Theoretical studies, utilizing the semiclassical oscillator model, have indicated that this is normally well into the region of validity of the quasistatic approximation (for atomic perturbers).[3] The internuclear separations which produce the observed radiation are less than 10 Å, so that binary collisions (or only diatomic molecules) predominately cause our spectrum at inert-gas densities below $2\times 10^{19}/cm^3$. Under these conditions, the quasistatic theory identifies the probability S of $\nu \rightarrow \nu + d\nu$ emission or absorption with the probability of finding a perturber in the $R \rightarrow R + dR$ region at the R that satisfies $h\nu = V_u(R) - V_l(R)$ (Fig. 1). In most statements of this relation the collision orbits are neglected and this probability is simply $n_0 4\pi R^2 dR$ (for diatomic interaction):

$$S(\nu)\, d\nu \propto \frac{n_0 4\pi R(\nu)^2 d\nu}{|d\nu/dR|} \quad . \tag{1}$$

When the correct collision paths or the internuclear distribution function are taken into account the perturber density n_0 is replaced by the density $n(R)$ in the neighborhood of a radiating atom. If the internuclear motion can be characterized by a single temperature that describes the bound and free distribution functions and the perturber density is much greater than the density of radiators,

then $n(R)$ becomes

$$n_0 \exp\{-[V_{\text{init}}(R) - V_{\text{init}}(\infty)]/kT\} .$$

In essence, this is the result used here to interpret the data. The ensuing material discusses the justification for this explanation, relates it to our experimental normalized intensity units, and allows for a variety of corrections such as for a changing dipole moment, statistical factors, and a nonequilibrated molecular population.

In the semiclassical model the perturbed atom radiates as a dipole whose frequency ν and strength are a function of the internuclear coordinate R. If this $h\nu(R)$ is identified as equal to the energy difference between two adiabatic molecular states which connect to the separated atom states, then this is equivalent to the classical Franck–Condon principle of vertical transitions. Jablonski derived Eq. (1), with the identification of ν just noted, for free-free transitions using JWKB wave functions and the stationary-phase approximation.[2] His results provide a valuable starting point, particularly since the accuracy and limitations of his approximations have been carefully investigated.[6,10] Jablonski's theory provides a quantum-mechanical justification for the normal classical quasistatic theory which assumes equal density of perturbers everywhere (equivalent to assuming straight-line collision trajectories). In addition it provides quantum-mechanical justification, if one is wanted, for describing the collision dynamics with classical collision trajectories. Jablonski calculated the Franck–Condon factors for an optical transition from a continuum state of total energy E in the initial diatomic electronic state to E' in the final. He noted that the dominant contribution to these Franck–Condon integrals occurred in the "stationary-phase" region, at the internuclear separation where the nuclear kinetic energies in initial and final states are equal and therefore the phase difference between E and E' wave functions changes gradually. By evaluating this contribution to the integral he obtained a result which we reproduce here from the integrand of Eq. (39) of Ref. 2:

$$S(E,\nu)\,d\nu = \left(\frac{4\pi R^3}{3}\right)^{-1} \left(\frac{\pi h^2(2l+1)\,dl}{2\mu E}\right) \frac{4\cos^2\phi\,d\nu}{[1 - V(R_c)/E - h^2 l(l+1)/2\mu E R_c^2]^{1/2}\,|d\nu(R_c)/dR_c|} . \tag{2}$$

This gives D^{-2} times the probability that a collision with nuclear angular momentum quantum number l occurs and causes an $E \to E' = E \pm h\nu$ transition, with absorption or emission at $\nu \to \nu + d\nu$. The perturber density, which we will call n_0, is $(4\pi R^3/3)^{-1}$; $V(R)$ and $V'(R)$ are the adiabatic potential in the initial final states, respectively; R_c is the position where $\pm h\nu = V'(R_c) - V(R_c)$; and D is the electric dipole strength at R_c. We have dropped a term ξ which allows for the inaccuracy of WKB functions near the classical turning point. More recent studies[10] have verified that Jablonski overestimated its importance in Sec. IX of Ref. 2. The phase ϕ is the phase-shift difference at R_c between upper and lower nuclear states [Eq. (36) of Ref. 2]; it is a function of l and E. The term in the second set of large parentheses becomes $2\pi\rho\,d\rho$ with change of variables $\rho^2 = \hbar^2 l(l+1)/2\mu E$, where ρ can be identified as the classical impact parameter [Eq. (27) or Ref. 2]. The factor $|d\nu(R_c)/dR_c|$ transforms a spatial differential from R_c to $R_c + dR_c$ into a frequency differential ν to $\nu + d\nu$. For classical motion with impact parameter ρ, the radial velocity at R_c is

$$v_R(R_c) = v(\infty)\left(\frac{1 - V(R_c)}{E} - \frac{\hbar^2 l(l+1)}{2\mu E R_c^2}\right)^{1/2} .$$

Thus Eq. (2) is equivalent to

$$S(E,\nu)\,d\nu = n_0\, v(\infty)\, 2\pi\rho\, d\rho \left(\frac{2\,dR}{v_R(R_c)}\right) 2\cos^2\phi . \tag{2a}$$

The terms in front of the large parentheses give the rate of classical collisions with impact parameter ρ to $\rho + d\rho$, and the term in the large parentheses gives the time spent between R_c and $R_c + dR$ for each collision. The $2\cos^2\phi$ is a quantum-mechanical interference effect with no classical interpretation, but when Eq. (2) is integrated over impact parameter and a distribution of collision energies these oscillations tend to be averaged out[6] and $\langle 2\cos^2\phi\rangle_{\text{av}} \to 1$.

If Eq. (2a), with $2\cos^2\phi = 1$, is integrated over the range of impact parameters that can contribute to the particle density at R_c, then multiplied by the Maxwellian distribution of collision velocities, it becomes

$$dS(T,\nu) = \frac{n_0\, 4\pi R_c^2\, dP_F(R_c, T)}{|d\nu(R_c)/dR_c|} , \tag{3}$$

where

$$dP_F(R_c, T) = \left(\frac{4[E - V(R_c)]}{\pi}\right)^{1/2} e^{-\beta[E - V(\infty)]}\, dE .$$

Here $\beta = 1/kT$, we have changed from velocity to energy variables, and the distribution of free perturbers at $R_c \to R_c + dR$ with energy $E \to E + dE$ is $n_0\, dP_F(R_c, T)\, 4\pi R_c^2\, dR$. The expression $4\pi R^2\, dR\, dP_F$ can be recognized[11] as the canonical distribution

$d^3p\,d^3R\,e^{-\beta E}$. The integral of $d^3R\,dP_F$ over momentum space, or over energy at fixed R as given in (3), leads to the canonical free-particle distribution in configuration space. In the case $V(R_c) > V(\infty)$, the energy integral extends from the minimum energy classically allowed at R_c:

$$P_F(R_c, T) = \int_{E_{\min}=V(R_c)}^{\infty} dP_F(R_c, T) = e^{-u}$$

(repulsive region), (4)

with $u = \beta[V(R_c) - V(\infty)]$. This is the expected equilibrium distribution since all particles classically allowed at R_c are free. In the case $V(R_c) < V(\infty)$, $E_{\min} = V(\infty)$ for zero momentum and (note $u < 0$)

$$P_F(R_c, T) = \int_{V(\infty)}^{\infty} dP_F(R_c, T) = e^{-u}\int_{-u}^{\infty} dy\,(4y/\pi)^{1/2}e^{-y}$$

(attractive region). (5)

In this case the free-particle distribution is not the entire equilibrium distribution. The portion of momentum space from $|P| = 0$ to $[2m[V(\infty) - V(R_c)]]^{1/2}$, corresponding to bound particles, has been excluded. The expression in (5) is the incomplete $\Gamma(\frac{1}{2})$ or the three-dimensional Gaussian error function. The $P_F[V(R_c), T]$ distribution is shown in Fig. 2, where it is compared to the equilibrium distribution. The difference between these free and equilibrium distributions is, of course, the bound-state classical canonical distribution $P_B(R_c, T)$. Figure 3 shows the kinds of intensity variations that these distributions predict for the experimental range of T.

Thus Jablonski's result applied to a thermal distribution of free perturbers is

$$S(T, \nu) = \frac{n_0\,4\pi R_c^2 P_F(R_c, T)}{|d\nu(R_c)/dR_c|}\ , \qquad (6)$$

with $P_F(R_c, T)$ given by Eqs. (4) and (5) and Fig. 2.

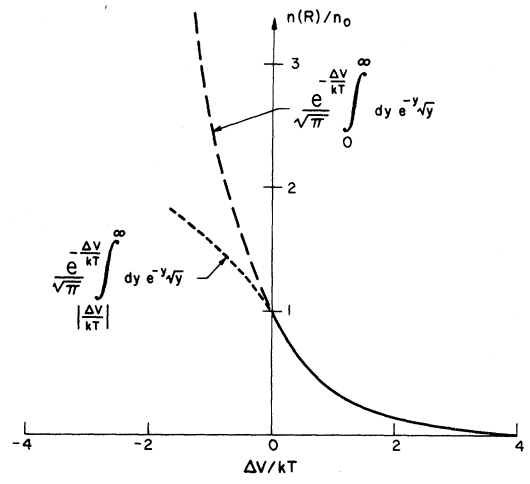

FIG. 2. Classical canonical distribution functions for an equilibrium ensemble (solid and long-dashed lines) and only free-particle collisions (solid and short-dashed lines).

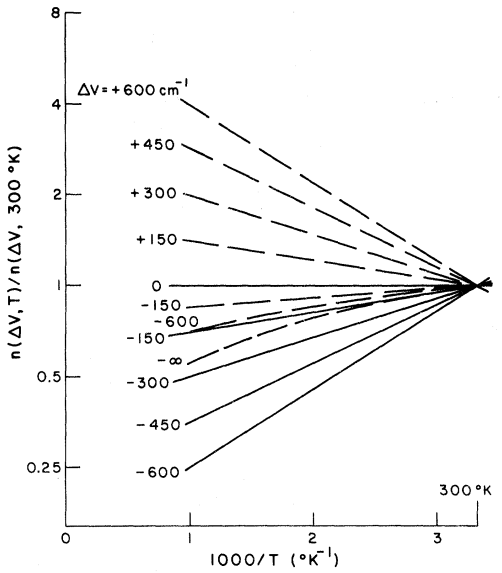

FIG. 3. Temperature dependence of $n(\Delta V, T)$ for the range of ΔV and T applicable in the experiment. [Taken from the $n(\Delta V, T)/n$ in Fig. 2.] The free-particle collision distribution is shown as dashed lines and the equilibrium distribution as solid lines.

This result applies to binary collisions between initially free particles, but we wish to draw a more general conclusion from Eq. (2) or (2a). As Jablonski noted, he was demonstrating the applicability of the classical Franck–Condon principle for free-free transitions. But as long as one excludes the lowest vibrational states where the quantum effects cannot be neglected, this principle is applicable to bound-free and bound-bound transitions as well. Indeed, Jablonski's JWKB wavefunction calculation could also be applied to bound states. If the initial adiabatic electronic state could support bound nuclear states, the thermal distribution of initial nuclear states would simply become the canonical distribution for bound and free states. In the present investigation we know experimentally that the wings do not show very significant quantum oscillations around average values, and it appears that there is no case where any portion of the spectrum is produced predominately by the first few vibrational states of a potential well. Consequently, we have interpreted our results entirely by the use of classical canonical distributions of free and bound perturbers in the initial-state adiabatic interaction potential. As we have noted, this provides the basis for a very

simple but effective interpretation of the data, and with possible minor exceptions it appears to be consistent with the considerable array of data presented below. In essence this is identical to the classical-oscillator quasistatic model with the addition of the classical canonical distribution of perturbers. We thus generalize (6) to

$$S(\nu, T)=\frac{n_0 4\pi R_c^2 P(R_c, T)}{|d\nu(R_c)/dR_c|} , \tag{7}$$

where $n_0 4\pi R_c^2 P(R_c, T)$ is the distribution of perturbers at R_c in the initial state of the observed transition. As noted above, this total distribution becomes $e^{-\beta u}$ when the canonical distribution of free and bound perturbers is included. In Appendix A, this is demonstrated in more detail for the experimental pressure conditions and various statistical factors are justified. The equilibrium distribution normally applies in an absorption experiment, but in our emission experiment the Cs* are optically excited as free atoms and bound Cs*–inert-gas molecules must be formed in competition with the Cs* radiative rate. The distribution functions appropriate to our experimental conditions are discussed in Sec. II D.

B. Normalized Emission Intensity

In an emission experiment Eq. (7) leads to a total emission intensity of

$$I(\nu, T)\, d\nu=\frac{N^* n_0 P(R, T) h\nu A(R) 4\pi R^2 d\nu}{|d\nu/dR|} . \tag{8}$$

Here N^* is the steady-state number of excited Cs atoms (free or bound to inert-gas atoms), $A(R)$ is the radiative transition probability, and $h\nu$ converts photons to intensity. In our experiment involving thermal collisions of a nonreactive species with Cs atoms, it appears very unlikely that the line strength S of the Cs resonance transition (with an oscillator strength near unity) can be modified by more than a small percentage, but the ν^4 factor between S and νA is quite significant for our extreme-wing radiation. We will assume below that S is constant since the adiabatic potentials differ from the free-atom energies by at most $\frac{1}{6}$ eV in the thermally accessible regions, whereas large percentage changes in alkali-metal-atom wave functions are needed to cause a significant change in the line strength. An indirect verification of this is provided by a calculation for the Li-Ne and Na-He systems.[12] For both of these cases the resonance-line line strength increased by only 8% at $3a_0$, a position where the $X\Sigma$ state was, respectively, ~0.3 and 0.5 eV repulsive.

In these experiments we collect a small solid angle of the radiation $I(\nu, T)$ in Eq. (8). The $^2P_{3/2}$ state fluorescence is initially about 15% polarized, but this is almost completely depolarized within the excited-state lifetime by collisions with the inert-gas atoms. Thus at the inert-gas pressures used $I(\nu, T)$ is isotropic and unpolarized and we sample a fixed percentage of it.

The Cs $6\,^2P_{3/2}$ state splits into two adiabatic states ($A\,^2\Pi$ and $B\,^2\Sigma$) in the presence of an inert-gas atom, so that Eq. (8) for two different components must be summed for the total radiation:

$$I(\nu, T)\, d\nu=\sum_i I[\nu_i(R), T]\, d\nu$$

$$=\sum_i \frac{N^* n_0 P_i(R, T) h\nu A_i(R) 4\pi R^2 d\nu}{|d\nu/dR|} . \tag{9}$$

Of course R and $|d\nu/dR|$ have an implicit dependence on i. At the pressures used in the experiment the integrated line intensity $I_0=\sum_i \int_0^\infty I_i(\nu, T)\, d\nu$ is produced predominantly within a few cm^{-1} of ν_0, where $A(R)\cong A$ the natural decay rate. Thus $I_0 = N^* A h\nu_0$ is a very good approximation. The Fabry-Perot monochrometer used for spectral analysis has a transmission T with about 15-cm^{-1} half-width and a flat top across the width of the resonance line at line center. Consequently when the filter is peaked at line center we detect

$$I'(\nu_0, T)=\sum_i \int_0^\infty T(\nu-\nu_0) I(\nu_i, T)\, d\nu$$

$$\cong T(0)\sum_i \int_0^\infty I(\nu_i, T)\, d\nu \cong T(0) I_0 . \tag{10}$$

From the known Lorentz broadening of line center,[4] it can be easily verified that the difference in these two integrals is less than 1% at the densities of $\sim 5\times 10^{18}/cm^3$ used for the wing normalization. The far-wing profiles reported here also represent less than 1% of the $\int k_\nu\, d\nu$ at these densities.

When the filter is centered at ν' we detect

$$I'(\nu, T)=\int_0^\infty I(\nu, T) T(\nu-\nu')\, d\nu .$$

If our filter width is narrow compared to the rate of curvature in $I(\nu, T)$ this integral is approximately

$$I(\nu', T)\int_{-\infty}^{\infty} T(\nu-\nu')\, d\nu = WT(0) I(\nu', T) ,$$

where W is the effective width of the filter [$WT(0) = \int T(\nu-\nu')\, d\nu$]. Thus when we scan our filter from the line wing to center we measure an intensity ratio of $WI(\nu, T)/I_0$. From Eq. (9) and the assumption $S(R)=S(\infty)$,

$$\frac{I'(\nu, T)}{I'(\nu_0, T)} = W n_0 \left(\frac{\nu}{\nu_0}\right)^4 4\pi R^2 \sum_i P_i(R, T) \left|\frac{d\nu_i}{dR}\right|^{-1} . \tag{11}$$

C. Distribution Function

For a gas in which collisional interactions dominate over radiative rates the population distribution in the states of nuclear motion reach equilibrium values for the kinetic temperature. (The

ratio of Cs* to Cs population is not in equilibrium in our experiment.) The classical distribution function for thermal equilibrium then reduces to (Appendix A)

$$P_j(R, T) = (g_j/g_f) \exp\left(-\frac{[V_u(R) - V_u(\infty)]}{kT}\right), \quad (12)$$

where g_f is the statistical weight of the isolated Cs*, and g_j of the molecular electronic state j. When atoms are excited in our experiment they will not be in an equilibrium distribution in the excited-state potential well, and their radiative rate will compete with equilibrating processes. Thus the equilibrium distribution function (12) holds for positive $V_u(R) > V_u(\infty)$ regions (if not inside a barrier) due to binary collisions, but not necessarily for negative regions. We have conducted this experiment at large enough inert-gas densities where the equilibrium distribution appears to hold for all bound states and free states of the Cs*–inert-gas pair. This has been established by measuring the temperature dependence of the wing intensity and comparing to the predicted equilibrium and free $P(R, T)$ functions. The results clearly agree only with an equilibrium $P(R, T)$ or something close to this. Also, at all regions of the well, the nonequilibrium distribution will have a smaller $n(R, T)$ than the equilibrated one. Consequently we have made other tests that are in essence a search for an increase in $I'(\nu, T)/n_0$ vs n_0 at wavelengths corresponding to the well regions. These tests are discussed with the data; it is our purpose here to set up a model that can be used to interpret these tests and the expected pressure dependence of the wing spectra.

It is not within the scope of this paper to elucidate details of the formation, destruction, and vibrational relaxation processes for Cs*–inert-gas molecules. Since we have interpreted our "high-pressure" experiments in terms of equilibrated distributions of bound and free molecular states, we require only a very crude collision model to interpret our experimental tests for nonequilibrated level populations. A realistic treatment would allow for the formation into a nonequilibrium distribution of vibrational and rotational states followed by collisional relaxation to an equilibrium population. The potential wells of the present experiments are not very deep, so we expect a fairly rapid equilibration once molecules are formed. From the standpoint of the radiated spectrum, the important feature of nonequilibrated populations is only the pressure dependence of the $n(R, T)$ probability distribution. We therefore consider a simplified case in which molecules combine directly into an equilibrium population distribution or are equilibrated very quickly after formation and maintained in this distribution by frequent level-mixing collisions. We use a single formation rate constant k_f to describe the formation of this equilibrium distribution and a single k_d for destruction of these bound molecules.

In addition, we are using a classical canonical distribution for the bound-state distribution. This averages through discrete quantum properties, and would be inappropriate if only a few bound states were filled. But in fact the Ar, Kr, and Xe potentials obtained from analysis of the data all have at least several vibrational levels within kT of the bottom and they are quite asymmetric in this region. Thus considerable vibrational and rotational averaging over quantum distributions is expected. In the He and Ne cases, where the vibrational spacings would be larger, the potential well is quite small. Thus minor oscillatory structures in the radiation spectrum might occur due to vibrational structure in the wells, but it should be superimposed on the average behavior described by the classical statistics. In addition, the quasistatic approximation for the spectrum neglects quantum effects so this might as well be extended to the distribution function in the present analysis.

The consequences of this model are calculated in Appendix A. The results, Eqs. (A19) or (A20) and (A21), demonstrate the expected competition between the radiative rate Γ_j and the molecular dissociation rate $k_d^j[A]$, where $[A]$ is the inert-gas density n_0. The classical equilibrium distribution function of Eq. (12) applies when $\Gamma_j/k_d^j[A] \ll 1$, and the free-particle distribution of Eqs. (4) and (5) when $\Gamma_j/k_d^j[A] \gg 1$. In an intermediate case our simple model predicts a reduction by $1+\Gamma_j/k_d^j[A]$ in the magnitude of the bound distribution, and thereby its contribution to the spectrum. A theory which included variations of k_d and k_f for different bound states in combination with vibrational and rotational relaxation would of course change the first term in (A21). Detailed studies at lower pressures than the present experiments are needed to take advantage of this as a diagnostic of these three-body rates. At present they are unknown and (A21) is used to explain the experimental criteria for an equilibrated distribution. We demand simply that the wing spectrum (normalized to line center) scale linearly with $[A]$, the inert-gas density. In some parts of these wing spectra the first integral in (A21) is more than an order of magnitude greater than the second, but in others it is zero. Thus both the magnitude and shape of the wing spectra can give a sensitive test for $\Gamma_j/k_d^j[A] \neq 0$. We, of course, cannot arbitrarily raise the inert-gas pressure to obtain molecular equilibrium since departures from the regime of only binary interactions are soon introduced. The pressure regime of the experiments is fitted between upper and lower bounds.

D. Potentials from Data

If $V_u(R) - V_l(R) = h\nu(R)$ is a monotonic function of R, Eqs. (11) and (12) can be used to obtain $V_u(R)$ and $V_l(R)$ from the data (except for an arbitrary constant). For reasons presented below, we believe each red wing for $\Delta\nu > 50$ cm^{-1} is produced by a single monotonic $\nu(R)$, allowing us to construct $V_u(R)$ and $V_l(R)$ from the data in the following manner. From the temperature dependence of $I'(\nu, T)$ we can obtain $P(R(\nu), T)$ for each ν. From Eq. (12) this yields $V_u(R(\nu))$; then $h\nu = V_u(R) - V_l(R)$ yields $V_l(R(\nu))$. The $I'(\nu, T)$ data are then extrapolated to $T = \infty$, where $P_i(T, \nu) = g_i/g_f$. Then

$$\frac{g_f}{g_i W n_0} \int_{\nu_1}^{\nu} I'(\nu', \infty) \left(\frac{\nu_0}{\nu}\right)^4 d\nu' = \int_{R(\nu_1)}^{R(\nu)} 4\pi R'^2 \, dR' = \tfrac{4}{3}\pi [R^3(\nu) - R^3(\nu_1)] , \quad (13)$$

where the left-hand side has been experimentally determined. Equation (13) simply notes that the radiation from ν_1 to ν corresponds to the volume from $R(\nu_1)$ to $R(\nu)$. Unfortunately this experiment does not independently determine $R(\nu_1) \equiv R_1$, and this one arbitrary constant remains in each pair of $V_u(R)$ and $V_l(R)$ functions. Nonetheless Eq. (13) gives $R^3(\nu, R_1)$ and since $V_u(\nu)$ and $V_l(\nu)$ are both known this yields $R^3(V_u, R_1)$ and $R^3(V_l, R_1)$. Atomic-beam scattering data for Cs ground state on inert gases allow us to establish R_1 is some cases to quite good accuracy by comparing our ground-state potential. Thus $R^3(V_u, R_1)$ and $R^3(V_l, R_1)$ can be inverted to yield $V_u(R)$ and $V_l(R)$. This procedure is demonstrated in detail in the analysis of the data.

E. Relation to Absorption Coefficient

Most line-profile measurements for neutral-gas broadening have been done in absorption rather than emission. In particular, very thorough measurements of the absorption coefficient for the Cs-Ar case studied here are now available[13] and it is useful to compare these with our results. The statistical factors and temperature dependences due to the unusually large frequency shifts are important, so we have elaborated on the relationship between normalized emission data and the absorption coefficient in Appendix B.

The first result, Eq. (B5), relates the absorption coefficient of a thermal vapor to the normalized emission from a vapor characterized by the same densities and kinetic temperature. But the electronic excitation temperature does not have to be thermal in the normalized emission measurement. Allowance is then made within the framework of the quasistatic theory for the effect of nonequilibrated excited-state distributions on k_ν. Combined with Eq. (11) for normalized emission this result, Eq. (B6), allows for comparison of absorption and emission data taken under varying conditions.

III. APPARATUS

The apparatus is designed to measure the wing intensity distribution of resonance fluorescence from optically thin Cs vapor due to interaction with inert-gas perturbers. The kinetic temperature of the vapor is varied from 300 to 800 °K, while the Cs density is maintained in the neighborhood of 10^{11} cm^{-3} and the inert-gas density at about 10^{19} cm^{-3}. The Cs is optically pumped with the $D1$ (8943 Å) or $D2$ (8521 Å) lines and the perpendicular fluorescence is measured from about 50 to 1000 Å from line center with about 15-Å resolution. A very-high-luminosity monochromator and cooled photomultiplier are used to detect these rather weak wing signals. The apparatus, shown in Fig. 4, and its relevant characteristics will now be described.

A. Cell and Gas Handling

The quartz cell is cylindrical, about 2 cm long and 2 cm in diameter and is connected to a metal-glass gas-handling system via a few cm of capillary tubing. An ampoule containing Cs is broken in the prebaked vacuum system. Cesium from the reservoir is distilled into the cell, or driven out of the cell by heating the cell in vacuum. Cesium is present both as vapor and as an absorbed layer on the cell walls; this absorbed layer acts as a local reservoir for Cs. Thus by transferring Cs in or out of the cell, the cell Cs density can be varied from zero up to the equilibrium vapor pressure at that particular cell temperature. In this way it is possible to obtain any desired optical depth of Cs independently of the cell temperature (though below room temperature the vapor pressure is not high enough to give adequate signal for the experiment). During an experiment the D-line fluorescence from the Cs is continually monitored by a photomultiplier and the intensity transmitted through the cell is monitored by a photodiode. Minor variations in Cs density as well as the effective optical depth are thereby monitored.

The cell is heated by flowing heated air past the cell inside a double-walled quartz tube that is evacuated between the walls. This arrangement minimizes pickup of blackbody radiation emitted by hot parts of the oven. Although the fluorescence due to lamp radiation is lock-in detected, the blackbody radiation is the primary source of photomultiplier noise at temperature above 150 °C. The temperatures of the upstream and (~10% cooler) downstream ends of the cell were measured with Pt/Rh thermocouples and an average taken. This

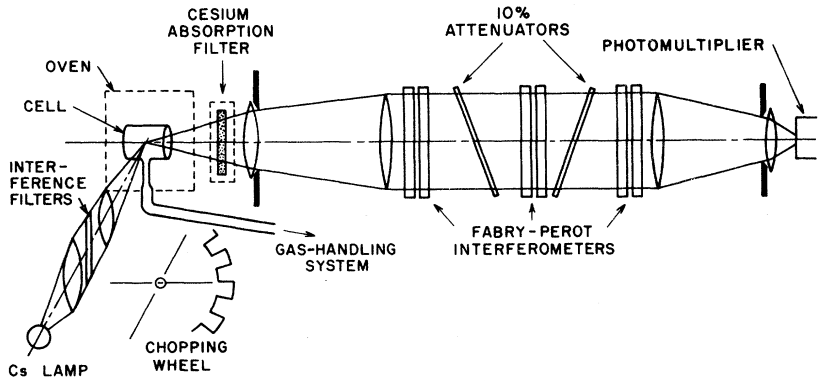

FIG. 4. Experimental arrangement.

procedure has been used to measure the very temperature-sensitive cross sections for excitation transfer by inert gases on Cs, and in spite of the temperature gradient and the measured cross sections agree with those from a uniformly heated cell.[14]

We have used research-grade bulbs and cylinders of inert gas. The gases are further cleaned by a flashed titanium getter before use. The gas pressure (20–500 Torr) in the cell is measured by nulling a capacitance manometer against an external mercury manometer. Impurity levels in the gas can be very sensitively measured by measuring $D2$ to $D1$ excitation transfer ratio, since the cross section for this transfer is 10^4 to 10^7 higher for polyatomic gases than for the inert gases for the temperature range of this experiment.[14] As an additional check on the contribution of impurities to the far-wing fluorescence we looked for wing emission from Cs broadened by $\frac{1}{10}$ Torr of N_2. Although this gives an excitation transfer ratio 20–50 times higher than we normally observe, there was no detectable wing emission.

B. Optics

The light source is an Osram Cs lamp (with jacket removed) in which the current and temperature can be independently controlled to produce a line shape that is efficiently absorbed by Cs vapor broadened by several hundred Torr of inert gas. Emission from the lamp is filtered through either of two D-line interference filters, chopped by a rotating slotted disc, and focused with $f:1$ optics into the quartz cell. Two separated filters are necessary since other lines from the lamp, typically those 50–100 Å on the blue side of the resonance lines, tend to leak through one filter at the larger angles to the optical axis and scatter off the cell and oven walls giving background signals. The D-line intensity irradiating the cell was about $\frac{1}{10}$ mW.

A monochromator was desired which was capable of scanning a range of 3000 Å with a resolution of about 10 Å. Also, since the line center is several orders of magnitude more intense than the line wings, the monochromator must have extremely low transmission outside its pass band. Furthermore, because of the very low wing emission intensity and the optical excitation of optically thin Cs, the detection system must be as fast as possible. To satisfy these requirements we employ three Fabry-Perot interferometers in series, each of different interorder spacing. Because the operation and properties of this device are rather complicated we describe it in greater detail below.

In addition to the monochromator, a number of other filters are employed. When examining the wing emission the very strong center emission is suppressed with a heated cell containing Cs vapor and about 100 Torr of argon. A reduction by typically a factor of 50 is obtained. The light absorbed in this absorption cell is eventually reradiated, but the detector receives only a very small fraction of the reradiation. By removing the inert gas from the fluorescence cell we could establish that the detector received no wing reradiation from the absorption cell. The minimum detectable signal for this test was about 10^{-3} as large as the normal wing fluorescence signals. On the other hand this result was quite sensitive to the absorption cell temperature or Cs vapor pressure. This was not always well controlled and possible errors due to this are discussed below.

Broad-band dichroic and interference filters were also used in certain wing regions to further suppress the line center. Since the monochromator passes radiation at wavelengths shorter than 7000 Å and longer than 11 000 Å, glass filters were used to block transmission outside these wavelengths. These also blocked long-wavelength blackbody radiation.

The detector is a dry-ice-cooled photomultiplier with $S-1$ response. The output of the monochrometer is imaged onto the room-temperature end of a quartz light pipe whose other end is cold and in contact with the photocathode envelope.

Only about 20% of the photocathode area is illuminated, and the effect of residual electron emission from the rest of the surface is reduced by means of a ring magnet placed around the light pipe. The photomultiplier output is ac amplified and lock-in detected at the chopper frequency. The dc output of the lock-in amplifier is integrated by an operational amplifier integrator and the slope of the integrated signal measured on a chart recorder. For the lowest signal levels (typically 3×10^{-7} of line center) an integration time of about 2 min was necessary for a signal-to-noise ratio of 1; the dark current was about 1000 electrons/sec and this signal was about 10/sec. At temperatures above about 300 °C the other source of noise is blackbody radiation from the oven and cell. Despite filtering by the monochromator and the other glass filters, this is the dominant source of photoelectrons and noise.

C. Triple Fabry-Perot Monochrometer

The cell fluorescence is isotropic from an illuminated region of about 1 cm in diameter and 2 cm long, a size that results from the lamp aperture of also about 1 cm. The wing fluorescence signals are quite weak, so that a very-high-luminosity spectrometer is desirable. Jacquinot has described luminosities of Fabry-Perot (FP) vs grating instruments; he finds the former much more luminous for normal instrument sizes.[15] Neglecting grating losses as well as FP absorption, our 70-mm-diam plates have about 100 times the luminosity of a grating spectrometer with 6×10-in. grating operated in first order. A single FP of course requires blocking of other orders, but several FP in series with various interorder spacings generally provide a useable instrument function without adding any more than some surface losses. Our three FP instrument uses dielectric coatings with reflectivities R of 0.90 ±0.02 from 7000–10 000 Å, and (mapped) single-plate flatness of about $\frac{1}{200}\lambda$. (The rms flatness variation, which better characterizes the instrument properties, was much less.) Although this flatness would not degrade the expected single FP reflectivity finesse of $R^{1/2}\pi/(1-R)\cong30$ at a wavelength where the reflectivity was 0.90, a value of 23 was typically measured. Further improvements in the plate-spacing techniques were made after the measurements described here. These improved the spacing flatness and repeatability and the measured finesse is now close to the expected value of 30.

The optical arrangement is indicated in Fig. 4. The two iris diaphragms in the focal planes of the internal lenses were adjusted to pass a portion of the central order sufficient to broaden the instrumental profile about 15%. The plates were typically operated with interorder spacings (free spectral range) of 240, 330, and 550 cm^{-1}. The over-all instrument response was measured by scanning the wings of the Cs resonance fluorescence without inert gas in the cell. The central part of such a scan is shown in Fig. 5. With 10% reflecting glass isolators between plate sets, the over-all transmission was close to the product of the three Airy functions. For about 1000 Å on either side of the trasmitted wavelength, the leakage varied from 4×10^{-4} to less than 10^{-6}, with an average value near 10^{-5}. The positions where one plate set was transmitting at adjacent order of course produced the larger (4×10^{-4}) leakages. The measured widths [W of Eq. (10)] were 21 ± 2 cm^{-1} at 8521 Å and 21.8 ± 2 cm^{-1} at 8944 Å, in agreement with the values calculated from the measured finesse of each interferometer and the product of the three individual transmission functions.

The interorder spacing of 200 to 500 cm^{-1} corresponds to plate spacings of 25 to 10 μm, so pressure scanning is out of the question. To ensure plate flatness and spacing accuracy, three points on the edges of each of the three plates were servo locked to the light from a grating spectrometer. One plate of each pair was mounted from differential screw micrometers and piezoelectric crystals at three positions. The output of the grating spectrometer was split into nine beams, each of which passed through the plates near one of the mounts. (The full plate size of 80 mm was coated and the outer 10 mm was used for the grating light.) Each servo system then adjusts the piezoelectric voltage on the adjacent mount to maximize transmission of the grating light. To compensate for imperfect plate flatness at the edges, the angle of

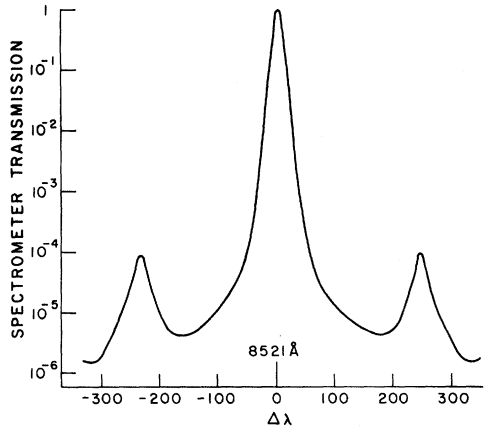

FIG. 5. Fabry-Perot spectrometer transmission function. The side peaks are an adjacent order of the set of plates with smallest interorder spacing. In the experiment a Cs absorption filter was used for an additional rejection factor of ~100.

each grating beam through the plates was adjusted until all central (70-mm) portions were flat and centered at the same wavelength. The three sets of plates are thereby flat and at the spacing determined by the grating spectrometer wavelength. The signal to noise in the servo loops was sufficient to easily follow a grating spectrometer scan rate of 50 Å/sec, and to settle with an rms noise level considerably below $\frac{1}{1000}\lambda$. In spite of these rather useful properties, we feel compelled to add a warning that constructing and aligning such an instrument is a job for patient men.

Part of the grating spectrometer light tended to scatter into the photomultiplier so that a shutter was placed over the photomultiplier while the plate spacings were locked; then this shutter was opened to take data after another shutter blocked the locking light beams. The piezocrystal voltages were held constant at the locked value while the data were recorded. Drifts in plate spacings due to temperature changes and relaxation in the piezocrystals could be kept negligible in the 2 min necessary to take a data point.

IV. MEASUREMENTS

The basic problem is to measure the collision-induced intensity $I(\nu, T)$ on the wings relative to the total fluoresced intensity for fluorescence from optically thin Cs. In addition, the interpretation of the data requires that we demonstrate the validity of binary interactions and thermally equilibrated excited-state populations. The measurements associated with these problems were divided into several parts. First the filter properties, background signals, and other instrumental properties were measured. The pressure regime for binary but equilibrated collisional spectra was established for what was expected to be the most restrictive case, xenon, due to the deep potential wells. The ratio $I'(\nu_1, T)/I'(\nu_0, T)$ was measured as a function of Cs density and temperature for a single point ν_1 on each red wing. Next, the ratios $I'(\nu, T)/I'(\nu_1, T)$ for the entire wing profiles were measured as a function of temperature. These measurements will now be discussed in more detail.

A. Instrumental

The measured wing intensities transmitted through the 20-cm^{-1}-wide filter were between three and six orders of magnitude smaller than the main fluorescence of the D lines. Consequently the optical filtering before and after the cell had to be carefully controlled to avoid errors due to filter leakages. Leakages of the D-line interference filters (between lamp and cell) allow other lamp lines to scatter off the cell walls into the monochromator. Although these leakages are independent of Cs and inert-gas density, they can obscure the desired wing signals. They were reduced with the double-filtering arrangement described with the apparatus, and the residual lines were corrected for or else their position on the wing was skipped over. (One leakage line about 10^{-5} times the D-line intensity was found on each blue wing, plus a few scattered lines that were much weaker.) The rejection of the monochromator and series blocking filters were checked by scanning the wings of the Cs fluorescence without inert gas in the cell. This was done with the Cs absorption filter in series with the monochromator to test for leakage lines from the lamp and wing fluorescence from the absorption filter. The total rejection of the FP and absorption filter was better than 10^{-7} (our noise level for a 5-min integration) at all $\Delta\lambda > 40$ Å under these conditions. This factor includes possible wing fluorescence by the argon-broadened absorption filter. The instrument function of the FP continues to apply when inert gas is introduced into the experimental cell, but the attenuation in the absorption cell decreases from more than 10^3 to typically 50 due to the broadening and shift of the line fluoresced by the cell. Owing to this and the overlap of secondary peaks of the triple-FP filter with the fluoresced wing radiation, broad-band interference filters were added for additional blocking starting about 500 Å on the red wings of the $D1$ and $D2$ lines and about 100 Å on the blue wings.

With Cs removed from the cell, the D-line scattering by the cell walls could be measured. The fluorescence signal from the Cs vapor was 12 to 50 times as large under normal conditions, so a wall scattering correction of 2–8% was needed to correctly normalize the wing intensity to the line-center fluorescence.

Since the signals $I'(\nu_0, T)$ at line center were many orders of magnitude larger than on the wing, a neutral density filter was used to attenuate these by about 10^3, and precision resistors were used to attenuate the photomultiplier signal by an additional 10 to 100 for comparison with the wing intensities.

The relative sensitivity of the detection system (glass blocking filter, FP, photomultiplier, and lenses) was measured across the 7000–10 000-Å range of the experiment so that the photomultiplier signals could be corrected to the actual fluoresced spectrum (Fig. 6). This was done by placing a white diffusing surface in front of the cell, illuminating it with a standard tungsten lamp, and scanning with the FP filters. The power spectrum of the lamp was known and the results were independent of the character of the diffusing surface (white paper, Teflon, titanium oxide paint), so this calibrates the relative response of the entire detection system. Broad-band interference filters were added in some regions to ensure against leakages

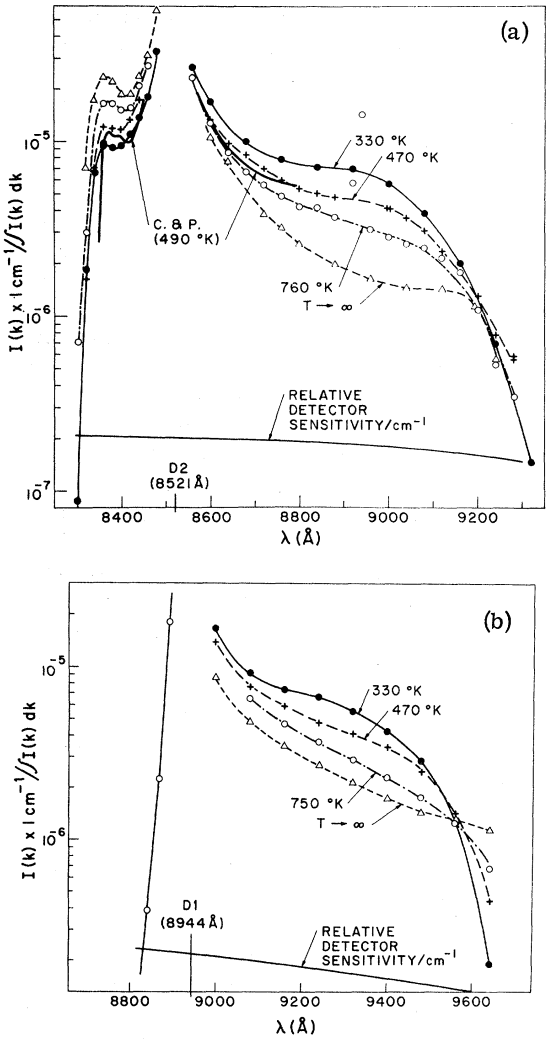

FIG. 6. Normalized fluorescence of the Cs $D2$ line (a) and $D1$ line (b) adjusted to $10^{19}/\text{cm}^3$ argon perturber density. These data are not yet corrected for the relative detector sensitivity shown. The line marked C & P represents the data of Ref. 13 converted with Eq. (B5) to normalized emission units. The $D1$ blue wing is less than the data shown, which is largely the instrument function of the spectrometer.

during this calibration. Since the FP coatings have (91 ± 1)% reflectivity across this entire wavelength range, the system response varied gradually and in a manner consistent with an S-1 photocathode and glass blocking filter.

B. Optical Depth

The Cs vapor is always optically thin in the wing regions studied, but the fluorescence at line center, which constitutes 99+% of the total fluorescence, may be reabsorbed before escaping the cell. A reabsorption affords another chance for a collision to produce radiation in the far wing. On the average this allows the wings to arise from the fluorescence of more atoms than does line center, and the detected-wing–to–total-fluorescence ratio increases with optical depth. The shapes of the wings are independent of this radiation trapping. The $I'(\nu_1, T)/I'(\nu_0, T)$ ratios were thus taken at small Cs optical depths, whereas the wing shapes were frequently taken under conditions where the line-center optical depth was near unity.

The dependence of $I'(\nu_1, T)/I'(\nu_0, T)$ on Cs vapor pressure was measured for the Kr $D2$ line at 200 Torr and 350 °K. The line-center fluorescence was used as an index of the Cs density, which was varied by changing the cell temperature. (The cell walls are a reservoir and sink for Cs, a 20 °C change typically alters the Cs density a factor of 2.) The Cs fluorescence could be normalized to a maximum value which occurs typically when about 70% of the pumping radiation is absorbed in the cell. Higher Cs densities cause major attenuation near the front edge of the cell, a region not imaged into the detector, and lower densities do not absorb as much of the available lamp radiation. The k_ν for Cs is of course broadened and somewhat shifted by the typically 5×10^{18} cm^{-3} density of inert gas, so its absorption is broad enough to encompass the lamp profile. It was found that a Cs density which yielded 40% of the maximum fluorescence produced about 10% increase in $I'(\nu_1, T)/I'(\nu_0, T)$, and data at lower densities were consistent with the same ratio. These figures are consistent with the following picture. The average escape distance for the fluorescence is about half the length of the cell traversed by the lamp radiation. At the Cs density which yielded 40% of the maximum fluorescence ~30% of the lamp radiation was absorbed and as a result ~15% of the fluorescence was reabsorbed. About $\frac{2}{3}$ of this reabsorption is in the region of the cell observed by the fluorescence detector, so roughly a 10% wing-to-center ratio increase would be expected. This argument assumes that the lamp profile is in the central portion of the k_ν for the Cs in the cell, so that the absorption probability for the lamp spectra is comparable to that for the fluorescence. If there were a serious mismatch, caused by a collisional shift that exceeded the broadening, the wing-to-center ratio would be further increased.

The $D1$ line has approximately half the absorption coefficient of the $D2$ line, but for convenience most $D1$ and $D2$ data were taken together at the same Cs density. The $D2$ fluorescence was kept between 20–40% of the maximum value, and the $D1$ was then between 10–20%. $I'(\nu_1, T)/I'(\nu_0, T)$ corrections of 5–10% and 2–5%, respectively, were applied to the data.

C. Binary Perturbations

The experimental results are interpreted as a binary process, involving only one inert-gas perturber at a time. By this we mean either the collision of a Cs atom with one inert gas (IG) at a time, or the formation of $Cs^*(IG)_n$ molecules with $n=1$ only and with negligible perturbation of these molecules by additional inert-gas atoms.

The binary regime applies when the probability of having more than one perturber within a volume $V_1=(4\pi/3)R_1^3$ around a Cs* or Cs*IG molecule is small, where R_1 is the greatest separation that will cause a significant perturbation. For our extreme-wing radiation the perturbation must be rather strong, say 30 cm^{-1}, before it can cause detectable changes from the binary spectrum. Owing to the weak interactions being considered and the fairly inert character of the perturbers, the magnitude of the two-body potential should be valid for this order-of-magnitude estimate of the effects of a third body. Then from our knowledge of the Cs*–inert-gas potentials, we can establish that this size perturbation occurs in the neighborhood of 6–8 Å for the various cases. For our typical inert-gas density n_0 of $6\times10^{18}/cm^3$ and $R_1=8$ Å, the probability is then about $n_0V_1=0.004$. This simple picture is complicated by the existence of attractive Cs*–inert-gas wells of depth $\Delta V>kT$. At equilibrium this alters the number of perturbers in the 0–8-Å region by approximately the volume average of $e^{-\Delta V/kT}$. This factor is as much as 3 for Cs-Xe ($A^2\Pi_{3/2}$) at room temperature, so perhaps a few percent divergence might be expected in this extreme case. Normally we expect to be well within the desired binary regime, even at the maximum inert-gas densities used of $2\times10^{19}/cm^3$.

We cannot lower the inert-gas density arbitrarily to find the binary limiting spectrum because this will prevent the formation of an equilibrated bound distribution of Cs*–inert-gas molecules. The pressure dependence of the Cs-Xe wing profiles at 320 °K were measured to test for both of these issues. Within some 5–10% uncertainty these profiles scaled with pressure from 4–15 $\times10^{18}$ cm^{-3}, supporting the applicability of the binary limit in this range where most of the data were taken for all of the gases.

D. Equilibrium Distribution Function

The other pressure-dependent process important in interpreting the results is the formation of bound Cs*–inert-gas molecules within the Cs* ($6\,^2P$) lifetime of some 3×10^{-8} sec. The temperature dependence in our red wing data fits an equilibrium distribution function for the Cs*–inert-gas density as a function of internuclear separation and is clearly too rapid to be produced by only free-particle collisions (Figs. 2 and 3). The Cs-Xe wing-shape measurements also support, within ~10%, the supposition that our lowest densities (4×10^{18} cm^{-3}) were high enough to form bound Cs*–inert-gas molecules and equilibrate these vibrational and rotational level populations. (We chose low temperatures and Xe for the measurements because it has the widest and deepest excited-state wells.) Since the 300–800-cm^{-1} red wing comes almost entirely from deeply bound states in the well but the blue satellite part of the line comes from free binary collisions, the ratio of red to blue wings is a very sensitive test of the molecular contribution. Noticeable decreases of 300–700-cm^{-1} red wing intensity relative to the blue satellite were observed only for densities below 2.5×10^{18} cm^{-3}. Details of the differences between the binary collision produced wings and those from an "equilibrated" population have been discussed in Sec. II. Although an oversimplified model was used there, it is sufficient to demonstrate that departures from the "equilibrated" distribution should cause significant changes in the wing profiles, and be easily detectable. The data are not sufficiently accurate to discount some minor departures from a completely equilibrated distribution of states in the well. Possible errors due to this are discussed below.

E. Normalization

As noted in Sec. IV B, the $I'(\nu, T)/I'(\nu_0, T)$ ratios were measured for a single wavelength on the red wing of each line. This ratio, indicated as $I(k)/\int I(k)\,dk$, where $k=\lambda^{-1}$, is plotted vs $1/T$ in Fig. 7. The $D2$ data have been corrected ~10% and the $D1$ data ~5% for the effect of the finite Cs optical depths (Sec. IV B). The straight-line fit corresponds to the expected $\exp\{-V_u[R(\nu)]/kT\}$ dependence. The slopes of the fitted straight lines give $V_u[R(\nu_1)]$, i.e., this establishes V_u at the R which is responsible for radiation at frequency ν_1. The extrapolations to $1/T=0$ normalize the size of the infinite-temperature wing data. A typically ±20% uncertainty in this extrapolated value is an obvious conclusion from the scatter in the data shown. This scatter is not due to photomultiplier noise; we believe it is due primarily to uncontrolled or undetected changes in the apparatus. One source later discovered was variations in the spectrometer effective finesse (plate spacings). Another was a gradual deterioration in the absorption cell window transmission.

F. Wing Shapes

The data described in Sec. IV E establish the wing-to-center intensity ratios as a function of temperature for one wavelength λ_1 on each red wing. The wing-shape data were then taken relative to this normalized wavelength. As noted in

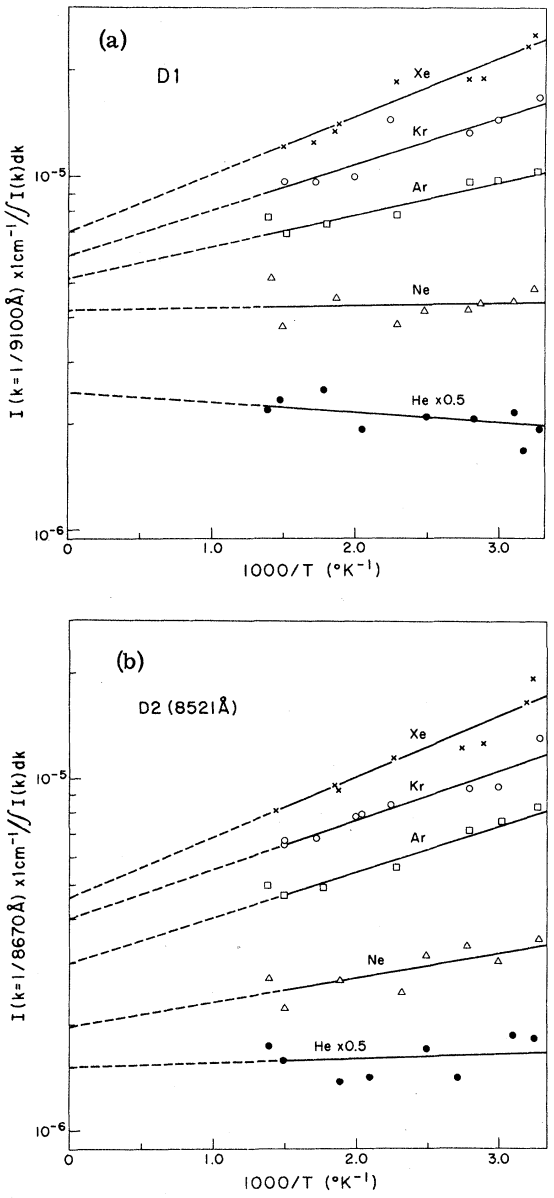

FIG. 7. Normalized wing emission data for single wavelength ($k = \lambda^{-1}$) on each red wing for (a) $D1$ and (b) $D2$.

Sec. IV B, the wing shapes are not effected by radiation entrapment and optical depths in the neighborhood of 1 were frequently used to increase the size of these wing-shape signals.

These data were also plotted as $I'(\nu, T)/I'(\nu_1, T)$ vs $1/T$ to establish the temperature dependence ($\nu_1 = c/\lambda_1$). From Eq. (9) these relative wing shapes are

$$\frac{I'(\nu, T)}{I'(\nu_1, T)} = \left(\frac{\nu}{\nu_1}\right)^4 \frac{4\pi R^2(\nu)\,|d\nu_1/dR|}{4\pi R^2(\nu_1)\,|d\nu/dR|} \frac{P[T, R(\nu)]}{P[T, R(\nu_1)]}$$

$$= f(\nu, \nu_1) \exp\left(\frac{-\{V_u[R(\nu)] - V_u[R(\nu_1)]\}}{kT}\right). \tag{14}$$

[Here again only one excited state is associated with the $R(\nu)$ or $\nu(R)$ on each $D2$ wing.] Thus exponential $1/T$ dependence is also expected for these ratios. Within the experimental uncertainty of typically ± 10% these data all fit a straight line or $e^{-K/T}$ dependence, as expected. In Fig. 8, we have shown one representative case, the argon $D2$ line. This is quite typical of the data for the other nine cases.

The slopes of the fitted lines in Fig. 8 give $V_u[R(\nu)] - V_u[R(\nu_1)]$. Combined with the $V_u[R(\nu_1)]$ from Fig. 7 these yield the $V_u(\nu)$, which are plotted versus $\Delta k = c(\nu - \nu_0)$ in Fig. 9. [In the quasistatic model, Δk is $\Delta(V_u - V_l)$ in cm^{-1} units.] Note that the temperature dependence in many well regions corresponds to the $V_u < -200\text{-cm}^{-1}$ line in Fig. 3, and is clearly much too rapid to be explained by the free-atom collisional distribution for any V_u.

The extrapolations to $1/T = 0$ in Fig. 8 yield the infinite-temperature wing shapes $I'(\nu, \infty)/I'(\nu_1, \infty)$. It can be seen that the accuracy of these extrapolated ratios in Fig. 8 is typically ± 10%, except at the rapidly dropping far edges of the blue and red wings, where it increases rapidly owing to spectrometer leakage and wavelength uncertainties. Combined with the extrapolations to $1/T = 0$ in Fig. 7, this gives the infinite-temperature wing shapes, normalized to line center, that are shown in Fig. 10. In order to show the whole picture, the argon wings are shown at several temperatures in Fig. 6.

V. ANALYSIS OF DATA

The blue wings of the $D1$ line decrease more rapidly than the edge of the FP transmission function for the plate spacing used. Consequently we obtained no useful information on these wings other than an upper limit on their size. (This absence of $D1$ blue wings is consistent with our model of the $A^2\Pi_{1/2}$ potential.) The $|\Delta\lambda| > 50$-Å blue wings of the $D2$ lines were resolved by the present filters, and the well-known blue satellites[1] are apparent. These indicate double-valued $R(\nu)$. The analysis of this wing therefore requires additional arguments and we defer them until the more straightforward red wing cases are completed.

In the case of the $6\,^2P_{3/2}$ state or $D2$ fluorescence two excited molecular levels ($B\,^2\Sigma_{1/2}$ and $A\,^2\Pi_{3/2}$) contribute to the wing fluorescence; the following analysis assumes that their fluorescence does not overlap in the wings. It also assumes a monotonic $V_u(R) - V_l(R) = h\nu(R)$ for the red wings. There are many aspects of the data which made a case in favor of this approach, but Baylis's potential calculations[7,16] were really the key element in convincing us to follow this approach to the analy-

sis. The accuracy of Baylis's excited-state potentials is difficult to assess *a priori*, but they would have to be completely altered to avoid the conclusions of a monotonic $\nu(R)$ on the red wings

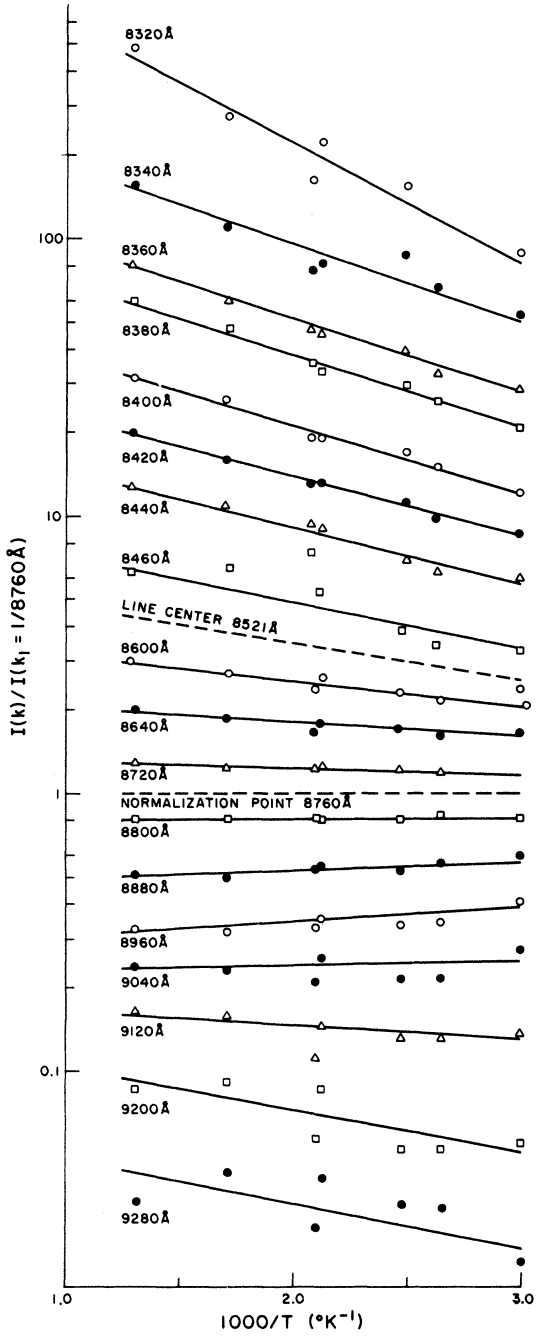

FIG. 8. Temperature dependence of the $D2$ wings due to $4-8\times10^{18}/\mathrm{cm}^3$ of argon perturbers. The data for each wavelength have been displaced vertically to avoid overlap. The temperature dependences are measured relative to that at 8760 Å. The 8760-Å temperature dependence relative to line center comes from Fig. 7.

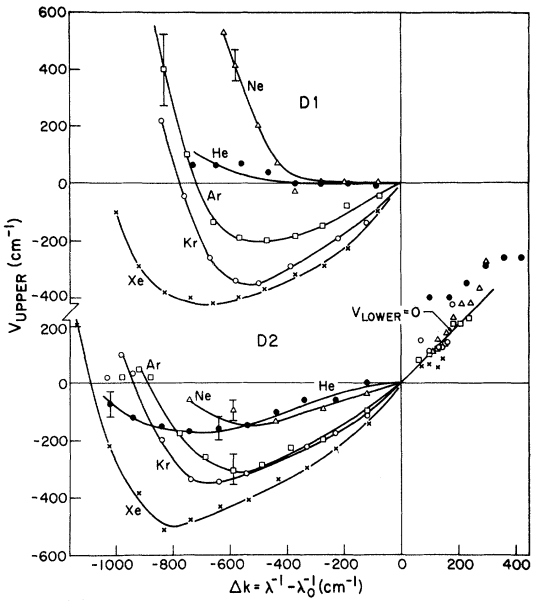

FIG. 9. The $A\,^2\Pi$ potentials (V_{upper}) vs the frequency shift in $\mathrm{cm}^{-1}(\Delta k)$ from the slopes of the data in Figs. 7 and 8, and the equivalent of 8 for the other cases. The quasistatic theory predicts $\Delta k = V_{\mathrm{upper}} - V_{\mathrm{lower}}$.

(for $\Delta\lambda > 50$ Å), and that the $B\,^2\Sigma_{1/2}$ and $A\,^2\Sigma_{3/2}$ states produce opposite wings of the $D2$ line. The potentials we obtain after making these assumptions are consistent with the assumptions, and appear to make a very strong case in their favor.

The next assumption used to reduce the data is that $P(R, T)$ is given by (12) at all R, corresponding to a classical equilibrium distribution of perturbers. As noted in Sec. IV, this appears consistent with all the data taken with inert-gas pressures between about 200 and 600 Torr, although we cannot rule out minor divergences from a complete equilibrated distribution. From these assumptions we obtained the $V_u(\nu)$ and $I'(\nu, T=\infty)$ data in Figs. 9 and 10. Since $h\nu = V_u - V_l$, the $V_u(\nu)$ also yields $V_l(\nu)$ or V_u vs V_l.

The $I(\nu, \infty)$ data are then integrated according to Eq. (13) to obtain the volume or R^3 as a function of ν, or $\nu(R^3)$ since it is a single-valued function. Combined with $V_u(\nu)$ and $V_l(\nu)$ from Fig. 9 this yields $V_u(R^3)$, $V_l(R^3)$ and $\nu(R^3)$. Again the argon example is shown in Fig. 11. This stage of the data reduction requires an assumption regarding the line strength vs R in the region that produces the spectrum. The assumption used to obtain Eq. (13) was a constant line strength. The error in this assumption is probably only a few per cent (see discussion in Sec. II A) and is not significant compared to experimental uncertainties. Note that an uncertainty in the magnitude or shape of the red wing profiles becomes an uncertainty in the R^3

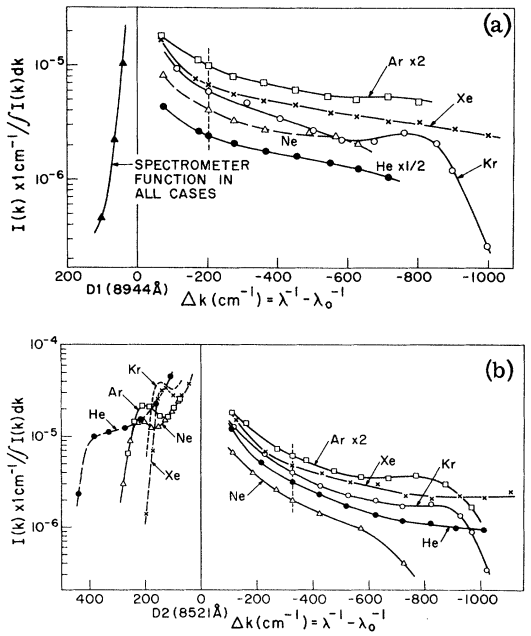

FIG. 10. Normalized infinite-temperature emission spectra for $10^{19}/cm^3$ perturber density. The experimental densities were $0.4-1.1\times10^{19}/cm^3$ and the spectrometer resolution about 20 cm^{-1}.

or volume scale of the potentials. An uncertainty in the temperature dependence, on the other hand, causes uncertainty in the relationship between V_u and V_l at each R. Subject to the quasistatic assumption $h\nu = V_u - V_l$, both V_u and V_l move up or down together if there is an error or uncertainty in the $V_u(R)$ of Fig. 7.

In order to specify $V_u(R)$ and $V_l(R)$ we must assign values $R_1 = R(\nu_1)$ for some ν_1 on the wing. An independent R_1 occurs for each red wing for each perturber gas. We have chosen to fix this point at the ν furthest from line center. This corresponds to the closest interatomic separations probed, and it is where the potentials are changing most rapidly with volume. For the Cs-Kr and Cs-Xe cases, we have chosen R_1 values by fitting to the $X^2\Sigma$ potentials from an atomic-beam scattering experiment.[17] Malerich and Cross have reported measurements for these two cases that establish the $X^2\Sigma(R)$ in the same repulsive region responsible for much of our data. Since this potential changes most rapidly in the most repulsive region the fitting is quite insensitive to even a ±100-cm^{-1} uncertainty in the $X^2\Sigma$ potential at R_1. The resulting potentials are shown in Figs. 12 and 13. Note that we obtain independent $X^2\Sigma$ potentials from the $D1$ and $D2$ wing data.

Baylis's calculation[7,16] has one arbitrary parameter (the cutoff radius about the inert-gas atom). He chose this parameter to fit the $X^2\Sigma$ well depth, which is known from atomic-beam scattering data. His calculation then predicts the entire $X\Sigma$, $A\Pi_{1/2}$, $A\Pi_{3/2}$, and $B\Sigma$ potentials. The repulsive region of his $X\Sigma$ potentials for Cs-Kr and Cs-Xe are in reasonable agreement with the Malerich and Cross data. Consequently it appears likely that Baylis's argon $X\Sigma$ potential should predict the repulsive region fairly well, and we have fitted our data to this to obtain the potentials in Fig. 14. For Cs-Ne and Cs-He the $X\Sigma$ well depths are very small and Baylis's method for choosing his cutoff parameter is questionable [the $V_u(R^3)$ and $V_l(R^3)$ data given here do provide the necessary information]. Consequently, we have simply noted that the fitted point in Figs. 12–14 at $X\Sigma = +1000$ cm^{-1} is 3.7, 3.52, 3.7 Å, respectively, for Cs-Ar, Kr, Xe. Based on implications from Baylis's calculations and possibly misplaced confidence in nature's regularity we have chosen slightly smaller values, 3.4 and 3.45 Å for the He and Ne cases. The resulting potentials are shown in Figs. 15 and 16. We hope it is clear that we are not asserting any accuracy for this fitted position. We merely wish to show the potentials in a form that is more familiar, rather than vs R^3. The volume plots can be easily constructed from Figs. 15 and 16 or the

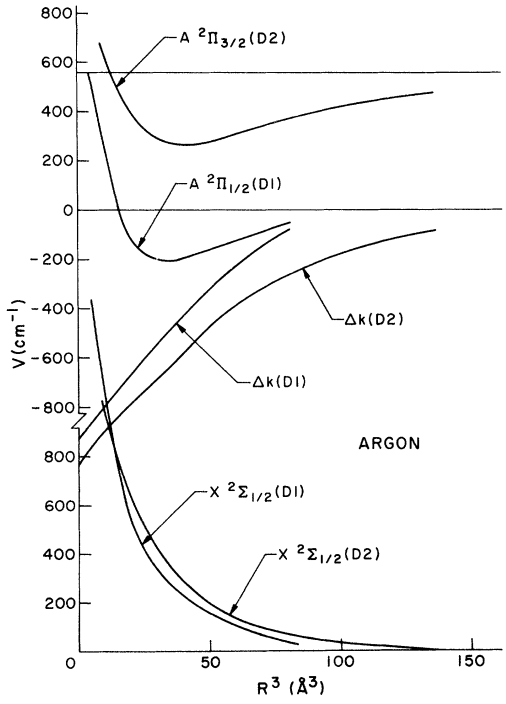

FIG. 11. Volumes associated with the potentials that produce the red wings, according to the quasistatic theory. These are obtained by integrating the data in Fig. 10 according to Eq. (13). Only the argon example is shown.

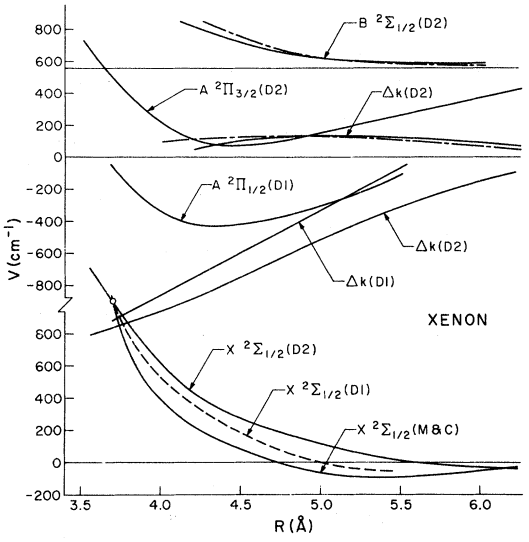

FIG. 12. The Cs-Xe adiabatic potentials obtained from the analysis of the data. An arbitrary radial constant is fixed by matching our $X^2\Sigma$ potentials to the atomic beam scattering potential from Ref. 17 at $R = 3.7$ Å (indicated by open circle). The potential marked (M&C) is from Ref. 17, those marked ($D1$) and ($D2$) are from our analysis of the $D1$ and $D2$ red wings. The $B^2\Sigma$ is from our analysis of the $D2$ blue wing. The quasistatic theory identifies $\Delta(V_{upper} - V_{lower})$ in cm^{-1} as the observed shift $\Delta k = \lambda^{-1} - \lambda_0^{-1}$. These $\Delta k(D1)$ and $\Delta k(D2)$ are included to show which R regions correspond to each part of the spectrum.

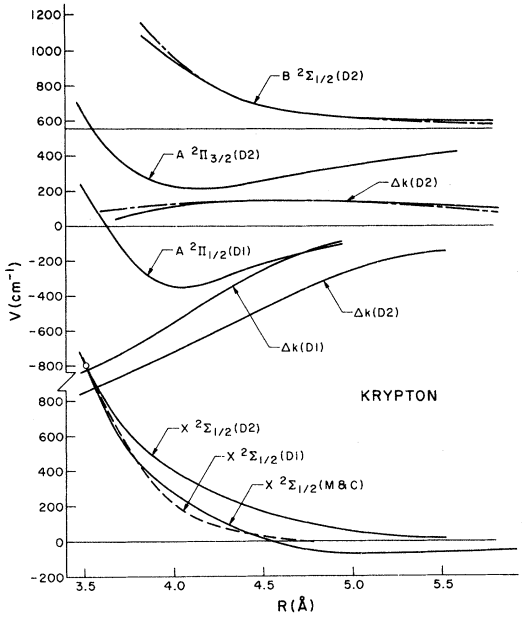

FIG. 13. The Cs-Kr adiabatic potentials. The notation is as in Fig. 12.

data in Figs. 9 and 10. In fact, one can save some time by noting that a small change ΔR_1 in R_1 is equivalent to shifting our $V(R)$ in Figs. 12–16 to $R + \Delta R_1[R_1/R]^2$. Across a limited R^2 range, this is just a translation of the entire curve.

The $D2$ blue wing appears to result from the $B^2\Sigma - X^2\Sigma$ transitions. The "satellite" indicates that $d(B\Sigma - X\Sigma)/dR = 0$ at some position. For this reason and because the temperature dependences of these wings are not sufficiently accurate, it would be difficult to establish much about the $B^2\Sigma$ and $X^2\Sigma$ potentials from only this blue wing data. Consequently, we will utilize the $X^2\Sigma$ potentials already established from the analysis of the red wings and beam scattering data. It is then possible to construct the $B^2\Sigma$ potentials from the $D2$ blue wing data. We proceed as follows.

Combined with the above $X^2\Sigma$ potentials, two quite dissimilar $B^2\Sigma$ potentials, each of which could produce the observed blue wing, are shown in Fig. 17. The $B^2\Sigma(2)$ potential is meant to be representative of a variety of such potentials that could be placed at large radial positions. Since the variations in $X^2\Sigma$ are gradual where the $B^2\Sigma(2)$ inflection produces the blue wing, the position of the $B^2\Sigma(2)$ curve is arbitrary. We have been able to concoct only one slightly feasible explanation for such a peculiarly shaped $B^2\Sigma(2)$ potential: the nonadiabatic mixing (V_{12}) of the $B^2\Sigma$ and $A^2\Pi_{3/2}$ states by the rotation of the molecular axis. At

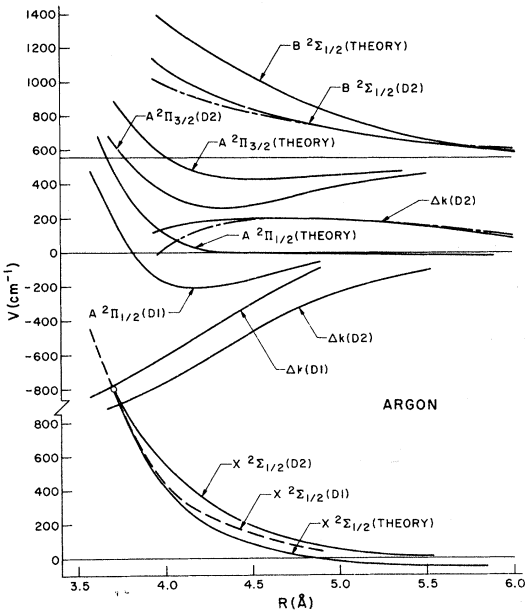

FIG. 14. Cs-Ar adiabatic potentials. The notation is the same as explained in Fig. 12, with the addition of the theoretical potentials from Ref. 16. The arbitrary radial constant in the data is chosen to fit the theoretical $X^2\Sigma$ potential at 3.7 Å (open circle).

the $10a_0$ region V_{12} would change more slowly with R than the adiabatic $B\,^2\Sigma$ and $A^2\Pi_{3/2}$ potentials, thereby repelling them by about V_{12} until their separation exceeded V_{12}. However, any inflections this could introduce into the final $B\,^2\Sigma$ potential would occur when it was less than V_{12} above the $R=\infty$ energy, and in addition the position of the inflection depends on velocity or temperature of the perturbers. Estimates[18] of the size of this V_{12} appear to be at least a factor of 10 smaller than the ~130-cm^{-1} shift of the Kr and Xe satellites. In addition we find that within an uncertainty of 10 cm^{-1} the position of the $D2$ blue satellites are independent of temperature. This peculiar $B\,^2\Sigma(2)$ potential is also clearly out of line with Baylis's adiabatic potentials, whereas $B\Sigma(1)$ is similar to his predictions.[16] Baylis did not include higher Cs*-Kr states in his calculation, but we think it very unlikely that any higher states could come down and cross through the $A\,^2\Pi_{1/2,3/2}$ and $B\,^2\Sigma$ states. (Such a mechanism has been suggested recently as a possible cause of some satellites.[19]) Amongst other objections, the consequences of

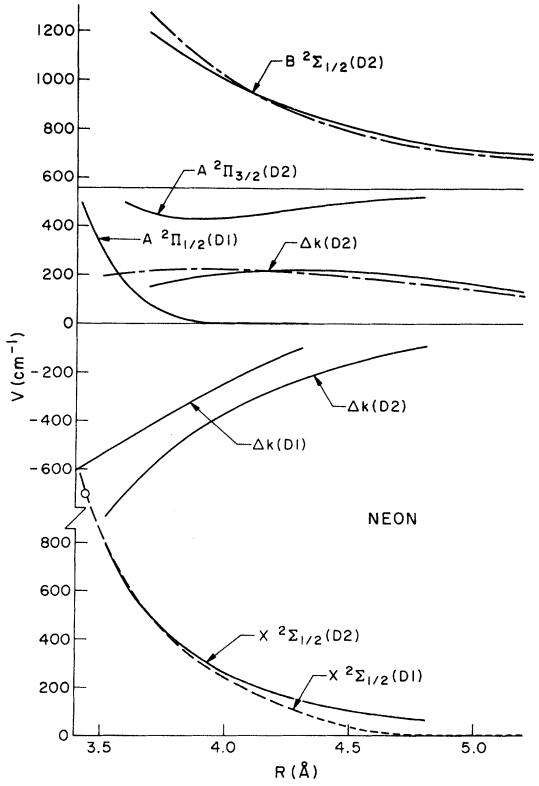

FIG. 15. Cs-Ne adiabatic potentials. The radial constants are arbitrarily chosen to put the $X^2\Sigma$ potentials through +1000 cm^{-1} at 3.45 Å. The notation is as in Fig. 12. The short-dashed part of the $X^2\Sigma$ $(D1)$ potential is an extrapolation of the data used to obtain the $B^2\Sigma$ potential in that region from the $D2$ blue wing data.

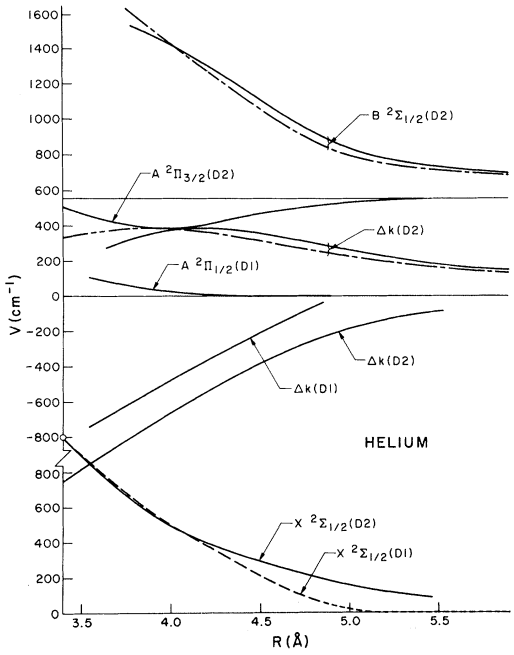

FIG. 16. Cs-He adiabatic potentials. The radial constants are arbitrarily chosen to put the $X\,^2\Sigma$ potentials through +1000 cm^{-1} at 3.40 Å. The notation is as in Fig. 12. The short-dashed part of the $X^2\Sigma$ $(D1)$ potential is an extrapolation of the data used to obtain the $B^2\Sigma$ potential in that region from the $D2$ blue wing data.

such crossings are grossly inconsistent with the experimental values and theoretical studies of the $6\,^2P_{1/2} \rightleftharpoons 6\,^2P_{3/2}$ excitation transfer cross sections.[14] We therefore focus our attention on the $B\Sigma(1)$ potential.

For this $B\,^2\Sigma(1)$ potential, $B\,^2\Sigma - X\,^2\Sigma = h\nu(R)$ is a maximum $(h\nu_m)$ at the satellite frequency and each $\nu_0 < \nu < \nu_m$ is produced by two radial positions. The contribution from either position is proportional to $P(R, T)\,dR^3(\nu)/d\nu$ so both regions contribute equally at $\nu = \nu_m$ but the $R > R_m$ contribution in-

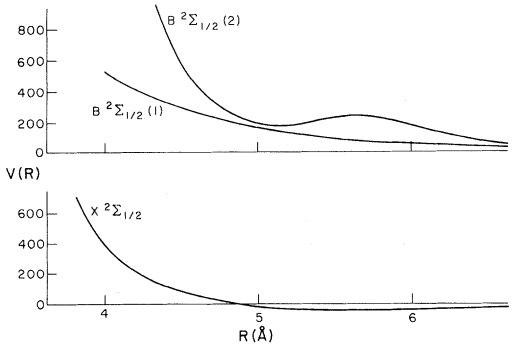

FIG. 17. Two types of $B\,^2\Sigma$ potentials capable of producing the $D2$ blue wings. Cs-Ar is used as an example.

creasingly dominates the spectrum as ν decreases from ν_m (Fig. 17). The temperature dependence is similarly a mixture of the $V_u[R_>(\nu)]$ and $V_u[R_<(\nu)]$ contributions, with the former dominating as ν decreases from ν_m. Our measurements were not sufficiently accurate to distinguish between this weighted sum of exponentials (vs $1/T$) and a single exponential at the properly weighted average potential. In principle the temperature dependence could be used to determine the ratio of $R_<(\nu)$ and $R_>(\nu)$ volumes for $\nu \rightarrow \nu + d\nu$, and thereby remove most of the ambiguity which results from the double valued $\nu(R)$. Our measurements are not sufficiently accurate to warrant this approach [a few % rather than 10–20% $I(\nu, T)$ uncertainty is required] so we have used the measured temperature dependence only for a consistency check. The $B\Sigma$ potentials have been established instead as follows.

The reported $D2$ blue wing satellites have a full width at half-height of typically 50 cm^{-1}. This smearing due to the finite collision time, finite pressures, finite filter width, and breakdown of the classical Frank–Condon principle must be removed for comparison with a zero-density quasistatic model. To do so we have integrated the $T = \infty$ blue wing data to obtain a volume-vs-ν plot (Fig. 18 shows the argon example). The quasistatic spectrum would have no volume past $\nu = \nu_m$, so we have then drawn an assumed line, labeled quasistatic equivalent in Fig. 18, that produces the same volume change from $\nu \leq \nu_m$. The exact position of this line is of course arbitrary, but it is hard to vary it enough to produce more than 20-cm^{-1} changes in the $B\,^2\Sigma$ potential obtained from it. The next issue is to divide this $\nu(R^3)$ into the sum of contributions from $R > R_m$ and $R < R_m$. At $R = R_m$ these are equal contributions and the $R > R_m$ part is increasingly dominant as ν decreases from ν_m. An assumed separation is drawn in Fig. 18. Here good temperature-dependent data could remove the ambiguity in this separation, but our data are sufficiently accurate to afford only a check on the separation used. Again it is quite difficult to concoct even slightly sensible separations which can alter the $B\Sigma$ potential by more than 10 or 20 cm^{-1}, except at the smallest R. In fact, if the separation in Fig. 18 is changed enough to make 20% changes in $B\Sigma(R) - B\Sigma(\infty)$, it generally leads to illogical $B\Sigma(R)$ shapes (e.g., with inflections or fluctuating curvature at small R).

The above steps lead to a single-valued $\nu(R^3)$ (Fig. 18). Just as with the red wing data the starting position R_1 for this volume is not known. But if we use the $X\Sigma$ potentials from the previous analysis there is very little uncertainty in the $B\Sigma$ potential due to this. The $B\Sigma$ potentials resulting from two choices of the R_1 position are shown in each of Figs. 12–16, along with the $\nu(R)$ or $\Delta k(R)$ which these produce. Choosing R_1 smaller than for these cases yields a $B\Sigma$ potential that flattens out at small R. Choosing a larger R_1 yields a $B\Sigma$ potential that does not converge towards $B\Sigma(\infty)$ at large R. In fact major changes in the assumed $\nu(R^3)$ separation in the assumed QS equivalent in Fig. 18 lead to similar catastrophes. There is suprisingly little freedom to juggle the $B\Sigma$ potential and still end up with the correct satellite position and volume. The temperature dependence in the satellite region is of course a further check on the $B\Sigma$ potential. These data are reasonably consistent with the potentials shown, although the typically ±50-cm^{-1} uncertainty in $V_u[R(\nu)]$ is insufficient for an accurate test.

The $X\,^2\Sigma_{1/2}$ potentials of Malerich and Cross[17] were used to obtain the $B\,^2\Sigma_{1/2}$ potential for the Kr and Xe cases. The theoretical $X\,^2\Sigma_{1/2}$ potential was used for the argon case. This was necessary since our $B\Sigma$ potential at large R is directly above the $X\Sigma$ well and its shape is quite sensitive to the $X\Sigma$ well depth. The $X\,^2\Sigma$ potentials from our red wing data have typically ±50-cm^{-1} uncertainty in this region, so they are not appropriate for fixing the $B\Sigma$ potential. For the Ne and He cases the theoretical potentials are less reliable owing to the necessity of fixing a parameter with the very shallow $X\,^2\Sigma_{1/2}$ well depths. On the other hand it can be inferred from scattering data that these $X\,^2\Sigma_{1/2}$ wells are at most 20 cm^{-1} for Ne and 10 cm^{-1} for He. Consequently, we have simply extrapolated our $X\,^2\Sigma_{1/2}(D1)$ potentials to zero as shown in Figs. 15 and 16, for the purpose of fixing these $B\,^2\Sigma_{1/2}$ potentials. Inaccuracies in any of the $X\,^2\Sigma_{1/2}$ potentials are of course carried directly into the $B\,^2\Sigma_{1/2}$ potentials.

VI. ACCURACY OF POTENTIALS

The model with which the data were analyzed allowed different parts of the data to be combined in a manner that averages through the fluctuations in individual data points. If one accepts the model, then the relevant question appears to be: How accurate are the potentials? If one questions the model, then the accuracy with which individual data points agree with a prediction of the model (using adjustable potentials) is relevant. We have already presented the available facts which support the validity of the model and the comparisons of the model predictions with the raw data can be easily made in Figs. 6–8. We will now address the issue of the uncertainty in the potentials due to uncertainties in the data but not the model.

First we consider the $A\,^2\Pi$ and $X\,^2\Sigma$ potentials from the red wing data. One issue that influences the accuracy of these potentials is the extent to which an equilibrium population distribution was

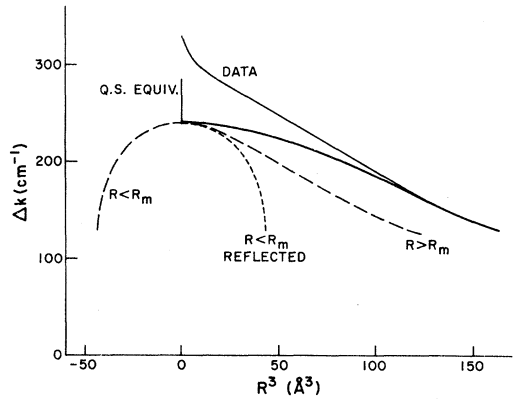

FIG. 18. Argon $D2$ blue wing data reduction, see Sec. V.

established in the excited states before radiative decay. If equilibration was incomplete, the intensity observed in the $A\,^2\Pi$ well regions would be too small, and the variations with temperature too slow. This would cause an underestimate of the well depth, an error which would be transferred to $X\,^2\Sigma(R)$ as well through $V_l = V_u - h\nu$; i.e., the correct potentials would be lower than the reported potentials in the R region covered by the upper-state well. The measured pressure dependence of the xenon wing shapes and the apparent $e^{-K/T}$ dependence of the wing intensity from the well regions are the evidence for assuming complete equilibration. On the other hand these data are not sufficiently accurate to discount the possibility of slightly unequilibrated bound populations and the other gases were not tested systematically. The fact that the $X\,^2\Sigma(R)$ from the $D2$ red wing are consistently higher than $X\,^2\Sigma(R)$ from the $D1$ line could be partly a consequence of an incompletely equilibrated bound distribution. (This cannot be the cause of the discrepancy in the He and Ne cases since it does not occur in the well region.) The deeper and wider $A\,^2\Pi_{3/2}$ well could cause it to be further from equilibrium and lead to this difference. A minor departure from equilibrium for $A\,^2\Pi_{1/2}$ and an increased departure for $A\,^2\Pi_{3/2}$ of Kr and Xe could explain the discrepancy from the $X\,^2\Sigma(R)$ of Ref. 17. Looking at it another way, perhaps the differences between $X\,^2\Sigma$ from the $D2$ and $D1$ lines and the Ref. 17 data provide a reasonable estimate for the magnitude of this uncertainty. On this basis $+0$, -50 cm^{-1} for $D1$ and $+0$, -100 cm^{-1} for $D2$ would be a safe allowance for $A\,^2\Pi_{1/2}$, $A\,^2\Pi_{3/2}$, and $X\,^2\Sigma$ well regions. Actually, we suspect that most of the discrepancy between $X\,^2\Sigma(D2)$ and $X\,^2\Sigma(D1)$ probably has other causes (e.g., normalization measurement errors) and this is an overestimate. The xenon pressure-dependence data do not seem to allow for more than $+0$, -50 cm^{-1} for $D2$ in the well region.

The potentials were established in two independent steps. $V_u(\nu)$ and $V_l(\nu)$ were found from the temperature dependence of $I'(\nu, T)$, while $R^3(\nu)$ and thereby $\nu(R)$ came from $I'(\nu, \infty)$. The data were taken in two separate stages, and each of these contributes an uncertainty to $V_u(\nu)$, $V_l(\nu)$, and $\nu(R)$. Considering first the $V_u(\nu)$ in Fig. 9, these values relative to the normalization point $[V_u(\nu) - V_u(\nu_1)]$ should be accurate to about ± 30 cm^{-1} except at the largest ν values where the intensity was dropping rapidly. The scatter was in fact somewhat worse on the $D2$ blue wings, mostly due to some problems with line-center rejection and background lines from the lamp. The $V_u(\nu_1)$ from the normalization data are less accurate, typically ± 50 cm^{-1}, as can be seen from Fig. 7. But an error here moves the entire $V_u(\nu)$ in Fig. 9 up or down, whereas we know that $V_u(\nu)$ should approach $V_u(\infty)$ in a reasonably uniform manner as $\nu \to \nu_0$. This can be used to discover an error in the normalization temperature dependence by utilizing the more accurate $I'(\nu, T)/I'(\nu_1, T)$ data (assuming one accepts the model). In fact we did shift the original He $D1$ $V_u(\nu)$ data -60 cm^{-1} and the Ne $D2$ $+30$ cm^{-1} in Fig. 9 on this basis. The temperature dependence of these $I'(\nu_1, T)/I'(\nu_0, T)$ data had sufficient scatter to be only slightly at odds with the readjusted fits. Over-all, the uncertainty in the potentials of Fig. 9 is about ± 30 cm^{-1} in the larger R regions, increasing to ± 100 or more near the smallest R's sampled. The self-consistency of the data varies considerably so this is meant as a rough over-all guide to the vertical uncertainties in Figs. 12–16. Of course, the $+0$, -50-cm^{-1} uncertainties in the $A\,^2\Pi$ well regions, noted in the previous paragraph, must be added to this.

The other uncertainty is in the volume scales which come from the $I'(\nu, \infty)$ data that were used to fix $\nu(R)$ or $R(\nu)$. Here the shape of $I'(\nu, \infty)$ is accurate to typically $\pm 15\%$ (Fig. 8) except at the largest ν values, but the magnitude of $I'(\nu_1, \infty)$ is determined by the less accurate extrapolations in Fig. 7. As a result a reasonable allowance for error would appear to be about $\pm 30\%$. This also becomes the uncertainty in the $R - R_1$ scale of Figs. 12–16; i.e., the relative scale of the potentials measured from the starting point at the smallest R is uncertain by typically $\pm 30\%$. It is apparent that this is sufficient to explain the major feature of the discrepancy between the $X\,^2\Sigma(D1)$ and $X\,^2\Sigma(D2)$. But since $X\,^2\Sigma(D2)$ is systematically higher, a systematic normalization error is implied. A greater optical depth correction is one possibility that cannot be completely discounted since this was tested only at one temperature and pressure for Kr $D2$ only.

The $B\,^2\Sigma$ potentials were not independently de-

termined, their accuracy depends on the accuracy of the $X^2\Sigma$ potential used. In the larger R regions of Figs. 12–16 these $X^2\Sigma$ potentials are known to ± 20 cm^{-1} or better from atomic-beam scattering measurements. The uncertainty in unfolding the $\nu(R > R_m)$ and $\nu(R < R_m)$ as well as in the smeared satellite adds perhaps ± 40 cm^{-1} to our $B^2\Sigma$ potentials in this region. [Actually if one recognizes the need for the $B^2\Sigma(R)$ to approach $B^2\Sigma(\infty)$ fairly uniformly this ± 40-cm^{-1} uncertainty is excessive.] At $R < R_m$ the $B^2\Sigma$ uncertainty increases rapidly; the dashed and solid lines in Figs. 12–16 give a reasonable indication of this.

Comparisons

The $X^2\Sigma$ potentials for Kr and Xe from the present experiments are less accurate than those from Ref. 17 in spite of the fact that their data do not uniquely establish the potential in the region between the well and perhaps + 100 cm^{-1}. Within our experimental errors there is not disagreement. For He, Ne, and Ar we are not aware of any other experimental data on the repulsive region of $X^2\Sigma$. The atomic-beam data have established the well depths and roughly their positions. Within our experimental errors we are in agreement with these well depths; we do not independently obtain the well positions. We are not aware of any other experimental determinations of the excited-state potentials.

The $X\Sigma$, $A\Pi$, and $B\Sigma$ potentials have been calculated *ab initio* for LiHe and for NaHe only.[12,20] Baylis has calculated these potentials for all the alkali-metal–inert-gas pairs using approximations based on the alkali-metal atomic wave functions and treating the inert gas as a polarizable dipole.[7] This polarizability attraction for the alkali-metal electron must be attenuated as the inert-gas electron cloud is penetrated; the procedure for cutting off this otherwise divergent contribution to the interaction energy leaves an adjustable parameter in the theory. This parameter has been adjusted to give a fit to the $X^2\Sigma_{1/2}$ well depth from atomic-beam scattering data. The calculations then yield predictions for entire $X^2\Sigma_{1/2}$, $A^2\Pi_{1/2,3/2}$, and $B^2\Sigma_{1/2}$ potentials. A set of potentials were published in 1968; further refinements in the method have led to a current set of potentials which show the same basic pattern but with important differences.[16] The early $X^2\Sigma$ potentials for Kr and Xe have a repulsive shape similar to the data of Ref. 17, but at about 0.3 Å smaller separation. The more current potentials are shifted to slightly larger separations. Baylis's early $A^2\Pi_{1/2}$ and $A^2\Pi_{3/2}$ potentials have well depths that are typically within 100 cm^{-1} of our data, but in the Kr and Xe cases where we can fix the positions they are at somewhat smaller separation, just as for the $X^2\Sigma$ potentials. (The radial position of our Kr and Xe potentials are fixed by the Ref. 17 data.) The current $A^2\Pi$ and $B^2\Sigma$ are systematically more repulsive than our data, typically by 200 cm^{-1} or more at 4-Å separation. The current argon potentials, which agree as well as any, are shown in Fig. 14. The experiment and theory are in agreement on the basic shapes, but the quantitative differences lead to very different predictions for the quasistatic spectrum. This disagreement is well outside of our experimental error. It is possible that inclusion of higher alkali-metal states in the calculation or a better method for cutting of the inert-gas polarizability could improve this.

The Cs-Ar profiles measured here can be compared, with the use of Eq. (B5), to the absorption coefficients measured by Chen and Phelps.[13] (We have used $A^{-1} = \tau = 3.2 \times 10^{-8}$ sec for the $D2$ line and 3.4×10^{-8} sec for the $D1$ line.[21]) This is done in Fig. 6. These k_ν measurements contain some uncertainty in absolute scale since they depend on the Cs vapor pressure. Earlier measurements of index of refraction for pure Cs in the same apparatus would appear to put this uncertainty in the 5% region. This, combined with accuracies of a few percent or less in their absorption coefficient measurements, should make the $k_\nu(T)$ results considerably more accurate than our $I(\nu, T)$ near line center. Further out on the red wings the absorption becomes quite weak and the uncertainty increases. The shape of the $D2$ wings are the same for both sets of data. As can be seen the magnitude of the blue wing peaks differ by about 15%, while the red wings are essentially in agreement. The $D1$ red wing absorption data (not shown) is about 25% larger than our data in the 9000–9200-Å region; there is no significant disagreement on the wing shape. These discrepancies are all well within the combined uncertainties of the two experiments.

VII. CONCLUSIONS

We believe that the experiments described here and the analysis method demonstrate a very powerful means of measuring interaction potentials of unstable molecules. The uniqueness available by unfolding these optical-continuum data exceeds that possible from atomic-beam scattering, and in addition we can investigate excited- as well as ground- or metastable-state interactions. The basic idea is to look at the continuum absorption or emission by atoms or molecules undergoing collisions. The spectrum maps the difference-potential surface and the velocity or temperature dependence maps the initial surface. The principal uncertainties are the variation in dipole moment and in the starting position for the volume to R step. This method can be applied to velocity- or

temperature-selected beams as well as vapors. Data-collection rates, for a given density and cross section, compare very favorably with those from atomic-beam scattering measurements. In essence, a typical collision time last 10^{-12} sec and a typical electric-dipole transition rate is 10^{-8} sec. Thus about 10^{-4} of the emission is in this continuum in a process such as chemiluminescence and about 10^{-12} $\mathcal{R}$ of the normal integrated absorption coefficient is distributed through this continuum, where $\mathcal{R}$ is the collision rate. With presently available tunable lasers for excitation and grating spectrometers for detection there are many reactive and nonreactive collision processes whose continuum spectrum can be investigated in beams as well as vapors.

The accuracy of the reported $I(\nu, T)$ measurements is typically at the 10–30% level, and this has limited the accuracy of our potentials to about ± 50 cm^{-1}. In addition we have insufficient data on the pressure dependence, which causes uncertainty in applying the equilibrated distribution function. These limitations are not imposed by the signal-to-noise ratios; they are simply the result of our first go around with the experiment. We cannot foresee any basic limitation which should prevent major improvements of accuracy in the immediate future. If this can be realized we believe this will be the most accurate method presently available for learning these interaction potentials, and perhaps many others as well. At that level of accuracy it will be necessary to investigate with more care the effect of the motion and pressure on the binary quasistatic spectrum, and the varying dipole moment. But these measurements will also yield the excited molecular dissociation and formation rates, combined with information on the relaxation rates within these bound states.

The $A\,^2\Pi_{1/2,3/2}$ and $B\,^2\Sigma$ potentials of the alkali-metal–inert-gas molecules are important determinants of at least three other processes that occur in buffered optical pumping cells. These processes, collisional depolarization, excitation transfer, and quenching have all been investigated experimentally and theoretically. We hope the potentials shown here will be useful in advancing our understanding of such processes.

ACKNOWLEDGMENTS

We wish to thank W. E. Baylis, who was associated with the early phases of this work, and A. V. Phelps for many helpful discussions and ideas.

APPENDIX A: BINARY-DISTRIBUTION FUNCTIONS

The free, bound, and total classical canonical distributions for Cs*–inert-gas (A) separations are evaluated here for the experimental conditions. The results are shown to be equivalent to directly applying the law of mass action to the Cs*, A, Cs*A system and using a classical form for the equilibrium constant. (The approach followed, rather than simply evaluating terms in the law of mass action, appears to be a more logical extension of the normal quasistatic-line-shape theories.) The consequences of the simple model for molecular formation and destruction are then evaluated.

(i) We first evaluate the canonical distribution of positions for a Cs* atom in a gas of $n_0 V$ inert-gas atoms randomly distributed in a volume V. The isolated Cs* electronic state has a degeneracy g_f and in interaction with the inert gas this splits adiabatically into electronic states j with degeneracies g_j and interaction potentials $V_j(R)$. The interaction potential in which the Cs* moves is thus

$$V_T = \sum_{j,i} \frac{V_j(R_i)\, g_j}{g_f} ,$$

where $R_i = |\vec{\mathrm{R}}_{cs} - \vec{\mathrm{R}}_i|$ is the separation from the ith inert-gas atom. The canonical distribution for the Cs* is then (Ref. 11, p. 149)

$$\frac{dN}{N} = \frac{\sum_j dN_j}{N} = \frac{q d^3R\, d^3\vec{p}}{h^3 q} \exp\left[-\beta\left(V_T(\vec{\mathrm{R}}) + \frac{P^2}{2M_{cs}}\right)\right] , \quad \text{(A1)}$$

where q, the partition function, is the phase-space integral of $q\,dN/N$ and we have defined subpopulations N_j for each electronic state j. Our experimental conditions correspond to binary Cs*A interactions, or equivalently to $\Delta V n_0 \ll 1$, where ΔV is the volume of the interaction region around one inert-gas atom in which $\beta[V(R) - V(\infty)]$ differs significantly from zero. Consequently $\beta V_T(R) \cong \beta V(\infty)$ over almost all of the volume and its variation can be neglected in calculating q. We then have

$$q = q_f e^{-\beta V(\infty)} \int d^3\rho\, e^{-\beta P^2/2M} \int \frac{d^3\vec{\mathrm{R}}}{h^3} = \left(\frac{2\pi M}{\beta h^2}\right)^{3/2} V g_g e^{-\beta V(\infty)} . \quad \text{(A2)}$$

For our low-pressure conditions, there are $n_0 V g_j / g_f$ independent potentials of type V_j in V_T. Thus from (A1) and (A2) the probability of a separation R from any one inert gas (regardless of the separation from all others) is[22]

$$\frac{dN_j}{N} = \frac{n_0 g_j\, d^3\vec{\mathrm{P}}\, d^3\vec{\mathrm{R}}}{g_f (2\pi M/\beta)^{3/2}} \exp\left[-\beta\left(V_j(R) - V_j(\infty) + \frac{P^2}{2M}\right)\right] . \quad \text{(A3)}$$

Here N refers to the entire Cs* population, which from the low-density arguments above (A2) is almost entirely free. For the distribution due only to free collisions we must integrate this distribu-

tion over the portion of momentum space that is accessible, $|P|_{\min}$ is zero, and we have

$$\frac{(dN_j)_F}{N_F} = \frac{n_0 g_j 4\pi R^2 dR\, e^{-u_j}}{g_f (2\pi M/\beta)^{3/2}} \int_0^\infty 4\pi P^2 dP e^{-\beta P^2/2M}$$

$$= n_0 4\pi R^2 dR\, P_j(R)_F ,$$

with

$$P_j(R)_F = e^{-u_j} g_j/g_f \qquad (u_j > 0) , \tag{A4}$$

where $u_j = \beta[V_j(R) - V_j(\infty)]$. This agrees with (4) in the case of only one interaction potential ($g_j = g_f$).

In the regions of attractive potentials

$$P_{\min}^2/2M = V_j(\infty) - V_j(R) ,$$

or $V_0 - V_j(R)$ for the region $R_0 - R_1$ of case C in Fig. 19. Thus

$$\frac{(dN_j)_F}{N_F} = \frac{n_0 g_j 4\pi R^2 dR\, e^{-u_j}}{g_f (2\pi M/\beta)^{3/2}} \int_{P_{\min}}^\infty 4\pi P^2 dP e^{-\beta P^2/2M}$$

$$= n_0 4\pi R^2 dR\, P_j(R)_F ,$$

with

$$P_j(R)_F = \frac{g_j e^{-u_j}}{g_f} \int_{-u_j}^\infty dy\, e^{-y} (4y/\pi)^{1/2} \qquad (u_j < 0) . \tag{A5}$$

This agrees with (5) in the case of a single potential.

The momentum space from $P = 0$ to $P_{\max}^2/2M = V_j(\infty) - V_j(R)$ represents the classical distribution of bound molecular states:

$$\frac{(dN_j)_B}{N_f} = n_0 4\pi R^2 dR\, P_j(R)_B$$

with (A6)

$$P_j(R)_B = \frac{g_j e^{-u_j}}{g_f} \int_0^{-u_j} dy\, e^{-y} (4y/\pi)^{1/2} \qquad (u_j < 0) .$$

Thus

$$P_j(R)_{\text{tot}} = P_j(R)_B + P_j(R)_F = e^{-u_j} g_j/g_f \qquad (u_j < 0) . \tag{A7}$$

Thus (A4) and (A7) give the expected equilibrium distribution at all R.[23]

The total number of bound molecules in this equilibrium distribution is

$$(N_j)_B/N_F = \int (dN_j)_B/N_F = n_0 Q_{N_j} ,$$

with

$$Q_{N_j} = \int_0^\infty 4\pi R^2 dR\, P_j(R)_B . \tag{A8}$$

N and $(N_j)_B$ are the total number of free Cs* and bound Cs*A_j, but their ratio is the same as the ratio of the concentrations. Using symbols [Cs*] and [Cs*A_j] for these concentrations and [A] for n_0, (A8) becomes an expression for the equilibrium constant

$$K_{\text{eq}}^j \equiv [\text{Cs}^*][A]/[\text{Cs}^* A_j] = 1/Q_{N_j} . \tag{A9}$$

We have discussed these distributions in the context of our experimental conditions, but for verification we note that (A9) is equivalent to the more familiar form of law of mass action (Ref. 11, p. 101):

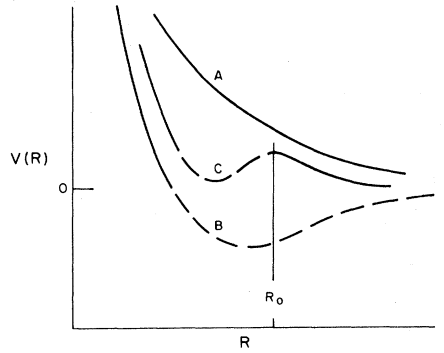

FIG. 19. Various $V(R)$ cases leading to free-particle and equilibrium distributions discussed in Appendix A.

$$\frac{[B][A]}{[AB_j]} = k_{\text{eq}}^j = \frac{(q_A)_{\text{Tr}} (q_B)_{\text{Tr}}}{(q_{AB_j})_{\text{Tr}}} \frac{q_A' q_B'}{q_{AB_j}'} , \tag{A10}$$

where $(q_i)_{\text{Tr}} = (2\pi M_i \beta/h^2)^{3/2}$ is the translational partition function and q_i' the internal partition function of molecular atom i. For our case of an inert gas for A and Cs* for B, $q_A' = 1$ and $q_B' = q_f e^{-\beta V(\infty)}$. The partition function q_{AB_j}' for the molecular state j is $g_j q_{Nj}'$, where q_{Nj}' is the partition function for the internuclear motion. We are approximating this internuclear distribution function with the classical or canonical distribution

$$q_{N_j}' \frac{dN_j(R_{12})}{N_j}$$

$$= \frac{d^3 \vec{R}_{12} \vec{d}^3 P_{12}}{h^3} \exp\left[-\beta \left(V_j(R_{12}) + \frac{P_{12}^2}{2\mu} \right) \right] , \tag{A11}$$

where μ is the reduced mass $M_A M_B/(M_A + M_B)$, q_{Nj}' is the integral of the right-hand side of (A11) over the momentum-space volume associated with bound molecules, the volume where $V_j(R_{12}) - V_j(\infty) = V'(R_{12}) < 0$ and $V'(R_{12}) + P_{12}^2/2\mu < 0$:

$$q_{Nj}' = \frac{e^{-\beta V_j(\infty)}}{h^3} \int_0^\infty 4\pi R_{12}^2 dR_{12}\, e^{-\beta V'(R_{12})} \times \int_0^{[-2\mu V_j'(R_{12})]^{1/2}} 4\pi P_{12}^2 dP_{12}\, e^{-\beta P_{12}^2/2\mu}$$

$$= e^{-\beta V_j(\infty)} \left(\frac{2\pi\mu}{\beta h^2} \right)^{3/2} Q_{N_j} . \tag{A12}$$

This, combined with the above q_A' and q_B', reduces (A10) to (A9). Indeed, we could have obtained all of Eqs. (A4)–(A9) by use of the canonical distributions for $[d\text{Cs}^*(R)]/[\text{Cs}^*]$ and $[d\text{Cs}^* A_j(R)/[\text{Cs}^* A_j]$ and the law of mass action. At higher pressures, the second virial coefficient and other corrections to the above q's would be more easily treated via the generalized q's of the law of mass action.

(ii) We now consider the simple model for the nonequilibrium situation. It is assumed that the molecular population is in the equilibrium distribution $P_j(R)_B$ of (A6), but $[\mathrm{Cs}^*A_j]$ may be below the equilibrium value of (A9). This means that

$$\frac{[d\,\mathrm{Cs}^*A_j(R)]}{[\mathrm{Cs}^*A_j]} = \frac{4\pi R^2\,dR\,P_j(R)_B}{Q_{N_j}} \quad . \tag{A13}$$

We define single formation and destruction rates for Cs^*A_j, R_f^j, and R_d^j, and specific rate constants k_f^j and k_d^j. These are of course functions of temperature with

$$R_f^j = k_f^j[\mathrm{Cs}^*][A], \quad R_d^j = k_d^j[\mathrm{Cs}^*A_j][A] .$$

These can be identified as equilibrium rate constants because the vapor has a well-defined kinetic temperature and the molecules have an equilibrium population distribution. We optically excite only one J state of $\mathrm{Cs}(6\,^2P_J)$, so $[\mathrm{Cs}^*]$ represents the entire concentration of free $\mathrm{Cs}(6\,^2P_J)$ with $g_f = 2J + 1$. (We will neglect the Cs nuclear spin.) The Cs^*A_j state must be adiabatically connected to the free $\mathrm{Cs}^*(6\,^2P_J)$. In fact there is one electronic state ($A\,^2\Pi_{1/2}$) of degeneracy $g_j = 2$ connected to the $\mathrm{Cs}^*(6\,^2P_{1/2})$ state with $g_f = 2$, and there are two electronic states ($A\,^2\Pi_{3/2}$, $B\,^2\Sigma_{1/2}$) each with $g_j = 2$ connected to the $6\,^2P_{3/2}$ with $g_f = 4$. Our experimental conditions correspond to optically pumping free Cs to free Cs*, at a steady rate per unit volume P_0. The inert-gas density at large separation from Cs atoms is about eight orders of magnitude greater than the Cs density, so it is unaltered by Cs–inert-gas or Cs*–inert-gas molecule formations. The pumping light is too weak to significantly alter the ground-state Cs population, and all excited M_J states are equally populated (due to depolarizing collisions). We have rate equations

$$\frac{d}{dt}[\mathrm{Cs}^*A_j] = R_f^j - R_d^j - \Gamma_j[\mathrm{Cs}^*A_j] , \tag{A14}$$

$$\frac{d}{dt}[\mathrm{Cs}^*] = \sum_j (-R_f^j + R_d^j) - \Gamma[\mathrm{Cs}^*] + P_0 . \tag{A15}$$

Under our steady-state conditions (A14) and (A15) give the total excited-state population

$$P_0 = \Gamma[\mathrm{Cs}^*] + \textstyle\sum_j \Gamma_j[\mathrm{Cs}^*A_j] \tag{A16}$$

plus the pressure dependence of $[\mathrm{Cs}^*A_j]/[\mathrm{Cs}^*]$,

$$[\mathrm{Cs}^*A_j]/[\mathrm{Cs}^*] = k_f^j[A]^2/(\Gamma_j + k_d^j[A]) . \tag{A17}$$

Equilibrium conditions apply when the radiative rate Γ_j is negligible compared to the destruction rate $k_d^j[A]$. In terms of the usual expressions for chemical equilibrium (A17) then becomes (Ref. 11, p. 101)

$$[\mathrm{Cs}^*][A]/[\mathrm{Cs}^*A_j]_{\mathrm{eq}} = k_d^j/k_f^j = K_{\mathrm{eq}}^j , \tag{A18}$$

where K_{eq}^j is given by (A9). The free collision distribution is given by (A5) and the molecular by (A6) and (A17). The total distribution is (using $k_f^j/k_d^j = Q_{N_j}$)

$$\frac{[dN_j]_T}{[\mathrm{Cs}^*]} = \frac{[d\,\mathrm{Cs}^*A_j]}{[\mathrm{Cs}^*]} + \frac{[dN_j]_F}{[\mathrm{Cs}^*]}$$

$$= [A]\,4\pi R^2\,dR\left(\frac{P_j(R)_B}{1+\Gamma_j/k_d^j[A]} + P_j(R)_F\right). \tag{A19}$$

In the repulsive or solid regions of potentials in Fig. 19, $P_j(R)_B$ is zero and

$$\frac{[dN_j]_T}{[\mathrm{Cs}^*]} = [A]\,4\pi R^2\,dR\,\frac{g_j}{g_f}\,e^{-u_j(R)} \quad (u_j > 0) . \tag{A20}$$

In the attractive regions $P_j(R)_B$ and $P_j(R)_F$ are given by (A5) and (A6):

$$\frac{[dN_j]_T}{[\mathrm{Cs}^*]} = [A]\,4\pi R^2\,dR\,\frac{g_j}{g_f}\,e^{-u_j(R)}\left[\int_{-u_j}^{\infty} \frac{dy\,e^{-y}(4y/\pi)^{1/2}}{1+\Gamma_j/k_d^j[A]}\right.$$

$$\left. + \int_0^{-u_j} dy\,e^{-y}\left(\frac{4y}{\pi}\right)^{1/2}\right] \quad (u_j < 0) . \tag{A21}$$

In the limit $\Gamma_j/k_d^j[A] \to 0$ the two integrals inside the large square bracket of (A21) sum to one, while the limit $\Gamma_j/k_d^j[A] \to \infty$ leaves only the second integral corresponding to the binary collision distribution. As originally assumed in the simple model, we have the sum of equilibrium molecular and binary distributions but with the total molecular population reduced. Equation (A21) gives the distributions and the reduction factor $(1+\Gamma_j/k_d^j[A])$.

APPENDIX B: ABSORPTION vs EMISSION

Detailed balancing requires that an equilibrium vapor absorb radiation of frequency $\nu \to \nu + d\nu$ from the thermal (blackbody) radiation field at a rate which balances the spontaneous emission into the same frequency range. If $\rho(\nu, T)\,d\nu$ is the thermal radiation field density then a unidirectional beam of intensity $c\rho(\nu, T)\,d\nu$ per unit area will produce the thermal field density and cause absorption that is balanced by the equilibrium spontaneous emission rate. From the definition of the absorption coefficient $[I_\nu(x) = I_\nu(0)\,e^{-k_\nu x}]$, the intensity absorbed in the volume of depth dx and unit cross-sectional area from a beam of intensity $c\rho(\nu, T)\,d\nu$ per unit area is $c\rho(\nu, T)\,d\nu \cdot k_\nu\,dx$.[24] Allowing dx to become a unit length, the absorption must equal the spontaneous emission intensity per unit volume, $I_{\mathrm{se}}(\nu, T)$:

$$I_{\mathrm{se}}(\nu, T) = k_\nu(T)\,c\rho(\nu, T) = k_\nu(T)\,\frac{8\pi h\nu^3}{c^2(e^{\beta h\nu} - 1)} . \tag{B1}$$

Equation (B1) is valid for any material at thermal equilibrium, but it is easiest to consider absorption and emission in a region of the spectrum where a single excited and ground electronic state of the free-radiator species dominates the spectrum. The generalization to overlapping lines is

clear, although not needed for the present experiments. These free-atom electronic states may of course split into different adiabatic states during interaction with the perturbers.

The k_ν and $I_{se}(\nu)$ spectrums of collisionally broadened lines must satisfy (B1) only at complete equilibrium, but with a slight additional step it can be applied to situations in which all states of nuclear motion are in equilibrium at temperature T but the electronic state populations are not. We note that under equilibrium conditions the ratio of the total populations N_u and N_l of the radiator electronic states is the ratio of their partition functions, but as in Eq. (A2) this reduces to the ratio of the free electronic or internal partition functions at low perturber pressures (lower than an atmosphere for less than 1% error in the present case). Then

$$N_u/N_l \cong (g_u/g_l)\, e^{-\beta h\nu_0} \ , \tag{B2}$$

where these are the statistical weights of the free atomic states.

Combining (B2) with (B1), we obtain

$$\frac{k_\nu(T)}{N_l} = \frac{c^2 g_u}{8\pi h\nu^3 g_l} \left(e^{\beta h(\nu-\nu_0)} - e^{-\beta h\nu_0}\right) \frac{I_{se}(\nu, T)}{N_u} \ . \tag{B3}$$

In an emission measurement where N_u is not the equilibrium value, the integrated emission intensity can be used to normalize the data, as in the present experiments. For allowed transitions and in the low-pressure limit this integrated intensity becomes

$$\int_0^\infty I_{se}(\nu, T)\, d\nu \cong N_u A h\nu_0 \ , \tag{B4}$$

where A is the spontaneous emission probability for the free-atom state u. In the present experiments this is a very good approximation at pressures below 1 atm.

Thus

$$\frac{k_\nu(T)}{N_l} = \frac{c^2 g_u A\nu_0}{8\pi\nu^3 g_l} \left(e^{\beta h(\nu-\nu_0)} - e^{-\beta h\nu_0}\right) \frac{I_{se}(\nu, T)}{\int_0^\infty I_{se}(\nu, T)\, d\nu} \ . \tag{B5}$$

(For the present experiments $e^{-\beta h\nu_0}$ is negligible.) Equation (B5) applies in the low-pressure limit to isolated lines of allowed transitions. It is clearly a thermodynamic result, and can be applied to plasma and discharge sources and molecular lines as well as the present experiments. Of course an actual experimental intensity is proportional to $I_{se}(\nu, T)$ only under optically thin conditions, and $k_\nu(T)$ and $I_{se}(\nu, T)$ in (B5) relate to the same perturber environment. If I_{se} and k_ν are measured at perturber pressures where binary collisions are dominant, they are both linear in perturber density and (B5) relates the reduced absorption coefficient $k_\nu/N_l n_0$ to the reduced normalized emission $I_{se}/n_0 \int I_{se}\, d\nu$. The temperature must be the same in the absorption and emission measurements, but not the densities N_l and n_0.

The states of nuclear motion in the ground electronic state should be in thermal equilibrium for almost any experimental situation, but this does not necessarily hold for excited states since radiative loss competes with collision rates. We have allowed for the effect of this on normalized emission intensity by using the quasistatic approximation, and we now note its effect on the quasistatic absorption coefficient:

$$k_\nu = \frac{C^2 A[R(\nu)]\, n_0\, 4\pi R^2 g_u}{|d\nu/dR|\, g_l} \left(N_l P_l[R(\nu), T] - \frac{g_l}{g_u} N_u P_u[R(\nu), T]\right) . \tag{B6}$$

---

*Work supported in part by the Advanced Research Projects Agency, The Department of Defense, and was monitored by U: S. Army Research Office – Durham, Box CM, Duke Station, N. C. 27706, under Contract No. DA-31-124-ARO-D-139.

†Present address: Department of Physical Chemistry, Cambridge University, Cambridge, United Kingdom.

‡Staff Member, Laboratory Astrophysics Division, National Bureau of Standards; Professor Adjoint, Department of Physics and Astrophysics, University of Colorado.

[1a]A preliminary report of this work was made by the present authors in Bull. Am. Phys. Soc. 15, 1528 (1970).

[1]S. - Y. Ch'en and M. Takeo, Rev. Mod. Phys. 29, 20 (1957); J. Cooper, *ibid.* 39, 167 (1967).

[2]A. Jablonski, Phys. Rev. 68, 78 (1945).

[3]T. Holstein, Phys. Rev. 79, 744 (1950).

[4]D. E. Gilbert and S. - Y. Ch'en, Phys. Rev. 188, 40 (1969); S. -Y. Ch'en, D. E. Gilbert, and D. K. L. Tan, *ibid.* 184, 51 (1969), with additional measurements referenced therein.

[5]J. M. Farr and W. R. Hindmarsh, Phys. Letters 27A, 512 (1968).

[6]F. H. Mies, J. Chem. Phys. 48, 482 (1968).

[7]W. E. Baylis, J. Chem. Phys. 51, 2665 (1969).

[8]G. Dunn, Phys. Rev. 172, 1 (1968).

[9]H. Hotop, E. Illenberger, H. Morgner, and A. Niehaus, Chem. Phys. Letters 10, 493 (1971).

[10]M. S. Child, Mol. Phys. 8, 517 (1964); W. H. Miller, J. Chem. Phys. 48, 464 (1968).

[11]N. F. Davidson, *Statistical Mechanics* (McGraw-Hill, New York, 1964).

[12]M. Krauss, P. Maldonado, and A. C. Wahl, J. Chem. Phys. 54, 4944 (1971).

[13]C. L. Chen and A. V. Phelps, Bull. Am. Phys. Soc. 15, 1528 (1970); details unpublished.

[14]A. Gallagher, Phys. Rev. 172, 88 (1968).

[15]P. Jacquinot, J. Opt. Soc. Am. 44, 761 (1954).

[16]W. E. Baylis (private communication) has introduced a number of refinements into the calculations described in Ref. 7. The results are not yet published.

[17]C. J. Malerich and R. J. Cross, Jr., J. Chem.

Phys. 52, 386 (1970).

[18]E. E. Nikitin, Opt. i Spektroskopiya 22, 379 (1967) [Opt. Spectry. USSR 22, 689 (1967)]; E. I. Dashevskaya and E. E. Nikitin, *ibid.* 22, 473 (1961) [22, 689 (1967)]; E. E. Nikitin, J. Chem. Phys. 43, 744 (1965).

[19]R. G. Breene, Jr., Phys. Rev. A 2, 1164 (1970).

[20]S. B. Schneiderman and H. H. Michels, J. Chem. Phys. 42, 3706 (1965).

[21]R. W. Schmieder, A. Lurio, W. Happer, and A. Khadjari, Phys. Rev. A 2, 1216 (1970); J. K. Link, J. Opt. Soc. Am. 56, 1195 (1966); A. Gallagher, Phys. Rev. 157, 68 (1967).

[22]This step is equivalent to $\Pi_i (1+f_i) = 1 + \sum_i f_i$ in the usual derivation of the second virial coefficient (p. 315, Ref. 11).

[23]J. O. Hirschfelder, C. F. Curtis, and R. B. Bird, *Molecular Theory of Gases and Liquids* (Wiley, New York, 1954).

[24]The relationship of k_ν to the Einstein B coefficient can be obtained by allowing a distributed $B(\nu)$. Then the absorption rate per unit volume is

$$h\nu[n_1 B_{12}(\nu) - n_2 B_{21}(\nu)] \cdot \rho(\nu, T)\, d\nu = k_\nu(T) c\rho(\nu, T)\, d\nu,$$

where n_1 and n_2 are the ground- and excited-state densities. Similarly a distributed spontaneous emission coefficient $A_{21}(\nu)$ can be defined by $I_{se}(\nu, T) = n_2(T) A_{21}(\nu)\, h\nu$. The normal Einstein A_{21}/B_{12} ratio is obtained only in the limit of a narrow line where $n_2/n_1 = g_2/g_1\, e^{-\beta h\nu}$ and $A_{21} = A_{21}(\nu)\, d\nu$, $B_{ij} = B_{ij}(\nu)\, d\nu$. In the absence of this condition the separation into $n(T)$ and $B_{ij}(\nu)$, $A_{ij}(\nu)$ is not justified. See A. C. G. Mitchell and M. W. Zemansky, *Resonance Radiation and Excited Atoms* (Cambridge U. P., Cambridge, England, 1934); the equation for k_ν on p. 95, combined with the detailed balancing condition $\rho(\nu, T)$ $(B_{12}\, dN_\nu - B_{21}\, dN'_\nu) = A_{21}\, dN'_\nu$, also leads to Eq. (B1). [Note that the B_{ij} on p. 95 and in Eq. (21) of Mitchell and Zemansky are $4\pi/c$ times the normal B_{ij}(density).] This separation of the total populations into components capable of interacting at ν is consistent with the quasistatic model but not valid in the general case.